Assemblies of hierarchical structures from anisotropically shaped colloidal particles

	Zhang Jie
	3
	17104 544
URL	http://hdl.handle.net/10228/00008901

Assemblies of hierarchical structures from anisotropically shaped colloidal particles

Thesis Submitted for the Degree of

Doctor of Engineering

By

Jie Zhang

Kyushu Institute of Technology, Graduate School of Engineering

Department of Engineering, Applied Chemistry Course

Assemblies of hierarchical structures from anisotropically shaped colloidal particles

Chapter 1. General introduction

Chapter 1. General introduction

1.1. Assemblies of colloidal particles

1.1.1. Colloidal particles and their assemblies

Colloid is a mixture consisting of a substance dispersed in another substance (called the medium). The dispersed substance is called colloidal particles. The colloidal particles are characterized by their size, at least in one dimension, between 1 nm and 1 μ m [1]. Because of their size, the colloidal particles are important members of nanoparticles or microparticles. They exhibit various interesting properties by themselves or after integration with other substances [2, 3]. Therefore, colloids are recognized as promising building blocks of novel nanomaterials.

For such application of colloidal particles, they are frequently required to be assembled into specific structures [4, 5]. With this process, the colloidal particles are hierarchically assembled to a larger scale, thereby exhibiting unusual functions based on particle-particle interactions in the assemblies [6, 7, 8]. Today, assembling of colloidal particles has been regarded as one of the most important key technology for fabricating novel advanced nanomaterials.

For assembling the colloidal particles, particle-particle interactions should be appropriately employed. Electrostatic and van der Waals interactions between the colloidal particles have been recognized as two important driving forces for this purpose in a classical theoretical regime called DLVO theory [9, 10]. With these interactions, the colloidal particles are weakly assembled in a solvent with keeping their dynamic nature, which enables construction of various nanoparticle-based materials such as thin films, porous solid, liquid crystals, gels, colloidal crystals [11, 12, 13, 14, 15], and so forth.

1.1.2. Importance of particle morphologies in the assemblies
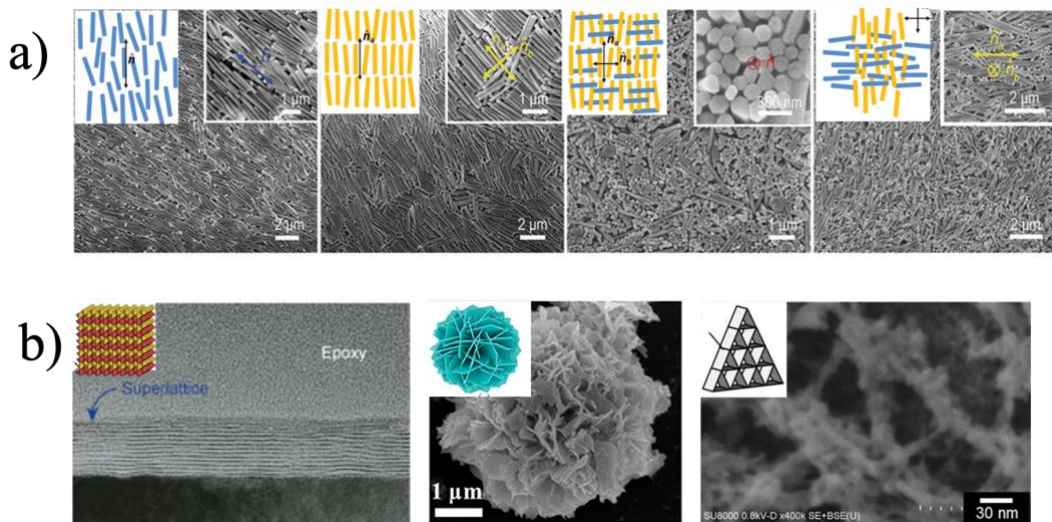
Figure 1.1. Typical structures assembled from anisotropic shape colloidal particles. (a) the structures assembled from one-dimensional rods [73]; (b) the structures assembled from two-dimensional sheets [74, 75, 76]

Although colloidal particles have been recognized as spherical or irregularly shaped for a long time, many recent studies have employed particles having shape

anisotropies such as 1D rods and 2D plates in colloidal systems [16, 17]. The shape

anisotropy greatly influences the structure of particle assemblies through asymmetric

particle-particle interactions. Meanwhile the shape anisotropy induces gradient of the

functions of particles because physicochemical properties of individual particles are not

spatially canceled in their anisotropic body.

*Figure 1.2. Schematic assemblies of pristine spherical colloidal particles and hybrid
particles*

Recently, numerous particle assemblies with broad structural diversity have been

organized by using anisotropic colloidal particles as shown in Figure 1.1, such as one-

dimensional rods and two-dimensional sheets, with similar assembly methods applied to

colloidal spherical particles. Comparing to assemblies of colloidal spherical particles as

shown in Figure 1.2, these anisotropic particle-based structures are hard to be achieved

from spherical colloidal particles because these assemblies have anisotropic structures

and anisotropic particle-particle interactions are necessary for their fabrication. Because

the spherical particles have isotropic shape and isotropic interactions between particles.

Thus, in recent years, colloidal assemblies of anisotropic particles are rapidly developed.

The particles can be assembled via various interactions such as electrostatic interactions,

van der Waals interactions, depletion force, capillary force, dipole-dipole attractions,

excluded volume effects [18,19], or some combinations of the above. Also, external force

such as shearing force, electric field, magnetic field [20], etc., are also effective for their

assemblies. Meanwhile, they can be assembled with templates into ordered structures [21].

1.1.3. Effects of the shape dimensionality of the particle on the assemblies

Anisotropic colloidal particles can be classified into 0D, 1D, 2D particles based

on their shape dimensionality. Nanodots, nanorod, and nanosheets are typical examples

of the 0D, 1D, 2D particles with different freedom of molecular motion and particle

assemblage as shown in Figure 1.3, respectively [60]. The difference in the shape

dimensionality offers several intrinsic characters on their particle assemblies. Typically,

the 1D and 2D particles tend to be assembled into 1D and 2D structures [22, 23]. When

these particles are manipulated with external forces, 0D and 1D particles can be
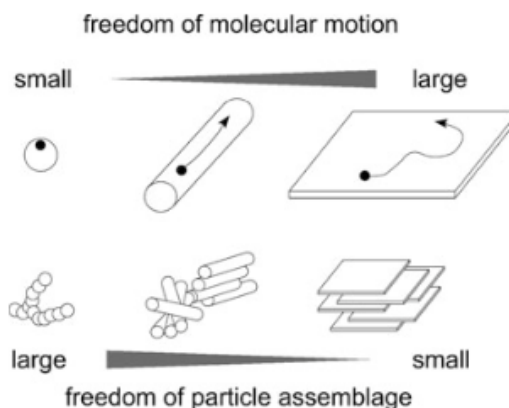
Figure 1.3. Schematic representation of the characteristics of 0D (dot), 1D (rod), and 2D (plate) particles and their freedom of molecular motion and particle assemblage dependency on dimensions [60]

unidirectionally aligned by a single external force. In particular, 1D particles can be organized with high regularity because of their uniaxial nature.   In contrast, unidirectional alignment of 2D particles cannot be attained under a single external force; the use of orthogonally applied two external force is necessary for such alignment [24].

1.2. Assemblies of 1D-shaped colloidal particles

1.2.1. Colloidal 1D-shaped particles

Colloidal one dimensional (1D)-shaped particles are those particles with two dimensions in nanoscale and one dimension out of nanoscale.   Depending on the shape and length scale differences within the particles, 1D-shaped colloidal particles can be classified into nanorod, nanotube, nanofiber, nanowire, and nanofilament [25, 26, 27, 28,

Nanotube   **Nanorod**   **Nanowire**

Nanofiber   **Nanofilament**
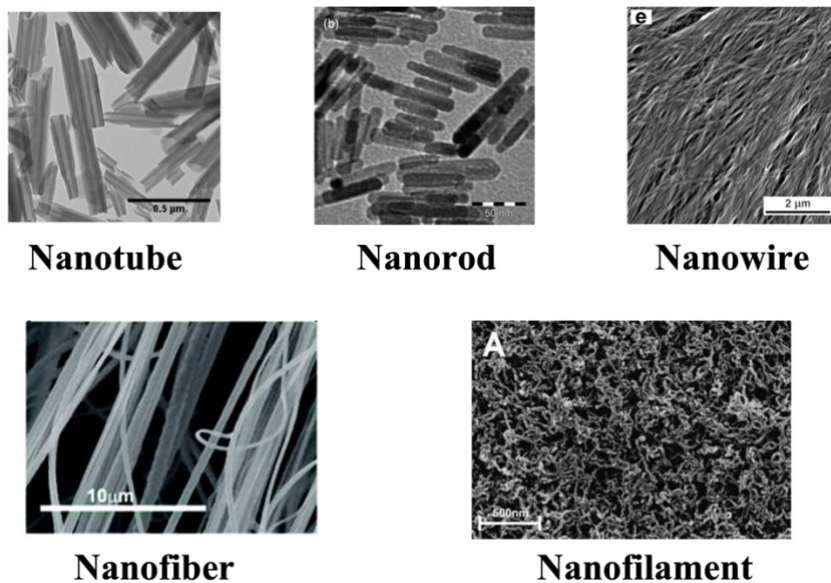
Figure 1.4. Typical 1D-shaped particles [25, 26, 27, 28, 29]

29], as listed in Figure 1.4. Both of inorganic and organic particles have been prepared as 1D particles as exemplified by Au nanorods, carbon nanotubes.

1.2.2. Principles of structure construction from 1D-particles

The colloidal 1D-shaped particles have been important building blocks for constructing novel structures applied in many areas such as electronics, photonics, biochemical sensing and imaging, drug delivery [30, 31, 32, 33], etc. Most of these applications require the well assembled structures. For the better application of these 1D-shaped particles into board areas with desired structures, the principles of how to assemble these 1D-shaped colloidal particles are critical.
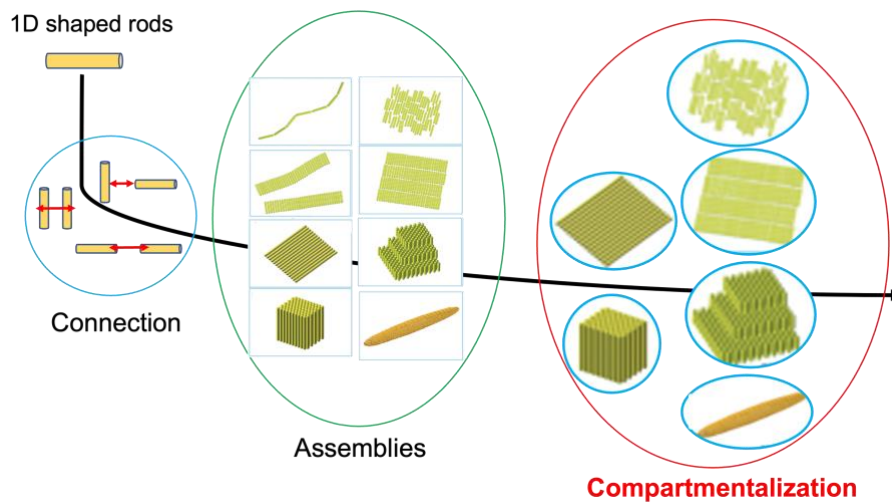
Figure 1.5. Schematic representation of 1D-shaped particle assembly principle and examples [77]

Common to the usual colloidal particles, these 1D colloidal particles can be assembled based on interactions in the colloidal system without the aid of external forces.

This process is called self-assembly [34]. For the case of 1D particles, however, the interactions are generally anisotropic reflecting the particle shape to facilitate formations of complicated superstructures in hierarchical manners. In this case, via controlling the interactions along the directional axis or perpendicular to the directional axis, these 1D-shaped colloidal particles can be connected in end-to-end or side-to-side manners as shown in Figure 1.5 [77]. They can be rather easily assembled to form various structures from micro to macroscopic scales as shown in Figure 1.5.

Application of external forces can effectively align the 1D particles at a macroscopic scale. As the external forces, electric and magnetic fields and shear force have often been employed for this purpose. The 1D particles are usually aligned with their longitudinal axis parallel to the applied force. The macroscopically ordered alignment of 1D rods can be immobilized in solid matrixes such as polymers to enable the application of the ordered structures as practical materials [35].

However, in many cases, for further application of these assembled structures, compartmentalization of these assembled structures is important as shown in Figure 1.5. In this case, the compartmentalization of 1D-shaped colloidal particle assemblies has arisen as a new general topic of 1D particles.

1.2.3. Cellulose nanocrystal and their assemblies

Cellulose nanocrystal (CNC) is one of the nanocellulose which cellulose with nano-scaled dimension. CNC is a 1D-shaped nanorod processing high crystallinity and characteristic surface with hydrophilic functional groups on their surface depending on how to make. CNCs are usually obtained by acid hydrolysis of cellulose with hydrochloride or sulfuric acid as shown in Figure 1.6, which remove amorphous parts via breaking the weak hydrogen bonding around the crystal cellulose, to obtain individual CNC [36]. Depending on the resource and preparation methods, CNCs with different chemical structures and size dimensions can be obtained [37]. In general, six interconvertible polymorphs are discovered in cellulose, where suballomorphs of Iα and Iβ are mainly discovered in native cellulose [38]. With repetitive packing of unit cells in nanorods, a twisted geometry is found in these CNC nanorods [39, 40]. CNCs range from 70 to 1000 nm in length and 3 to 50 nm in width [37].
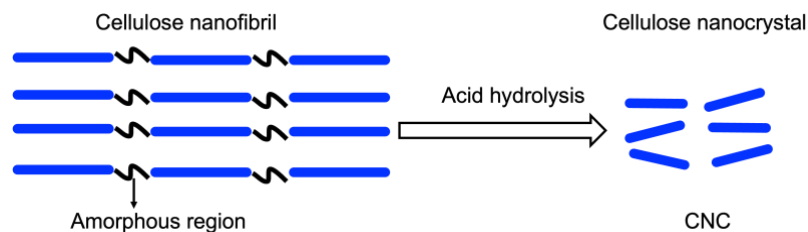
Figure 1.6. Schematic process for cellulose nanocrystal preparation with acid hydrolysis

CNC nanorods are attracting more interests in recent years since they are natural-

based materials, which can be used as sustainable, biodegradable building blocks comparable to those by synthetic polymers. More importantly, these CNC nanorods can be assembled into chiral nematic manner in water forming a liquid crystal state, which is supposed to be induced by twisted shape of the nanorods. The chiral alignment in left-handed manner can be preserved in dried film as shown in Figure 1.7 [41, 42]. This characteristic gains much attention and many studies focused on this property is reported in recent years [42, 43]. Thus, in addition to the interactions as usual 1D nanorods, CNCs also have potential to be assembled into more complex manner, i.e., chiral nematic manner.

Furthermore, hybridization with other materials with CNCs are also studied by many researchers. Inorganic and polymer materials are often hybridized with CNC to make functional composite [44, 45]. In general, composite with polymer can attain softness and compatibility with other polymer matrixes. Polymer composite can show unique mechanical behavior based on intrinsic high mechanical property by CNC [46, 47] and can be compatible with other hydrophobic materials because CNC surface itself have hydrophilic characteristics [47, 48]. Fabrication of CNC-polymer composite is important category for CNC composite, however, the most of the researches for the composite are carried out for large scale systems including CNC chiral nematic films [49, 50, 78] and

CNC unidirectional fibers [79], as shown in Figure 1.7.
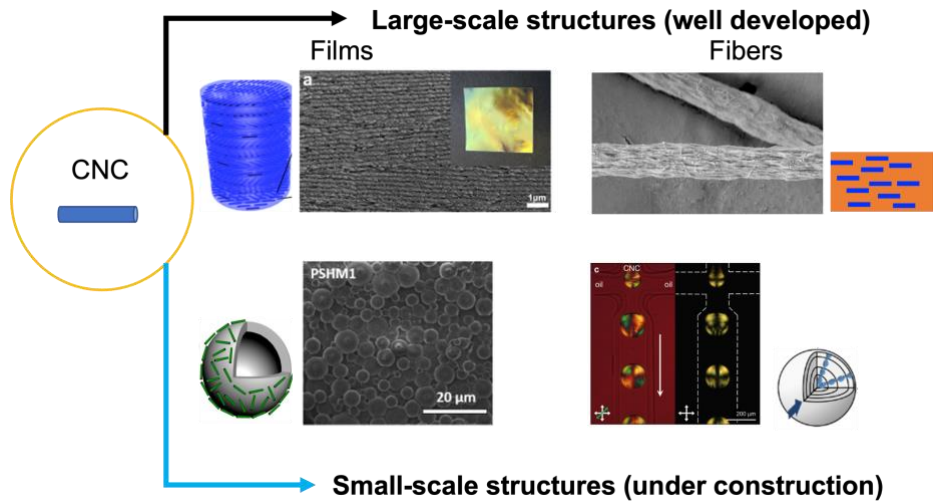
Figure 1.7. Typical assemblies of CNCs includes large-scale structures in form of films and fibers [78, 79]; and small-scale structures in form of core-shell particles [51, 52]

Among the CNC-polymer composite, composite capsules, as shown in Figure 1.7, are a new class of CNC materials although the number of reported studies is limited. Comparing with other types of composites, these capsule composites are small scale structures. They are specific in the sense of size. They are usually micro-sized particles and own distinct structures inside each particle. There are studies in which CNC component can be either core or shell constituent while the other part is composed of polymer constituent [51, 52]. There also has another case that both CNC and polymer can be shell with empty core [53]. These CNC-polymer core-shell particulates have specific features of sized controlled isolated space, which is expected to be an important part of CNC based materials. Comparing to the large-scaled structures, these small-scale

structures are important to hand and incorporate such assembled structures in integrated

systems. In this case, compartmentalizing CNC by particulate assemblies should be

important to make new building blocks in order to realize hierarchical assemblies with

independent control in each hierarchy.

1.3. Assemblies of 2D-shaped colloidal particles

1.3.1. Colloidal 2D-shaped particles

Colloidal 2D particles are anisotropic particles with platelike morphology, where two

dimensions are out of nanoscale and one dimension is in nanoscale.   Nanosheets, nanoplates,

and nanodiscs [54, 55, 56] are examples of 2D particles, as shown in Figure 1.8.   Typical

materials obtained as 2D particles are Au sheets and graphene sheets [56].   These particles are

prepared by bottom-up strategy through polymerization of monomeric inorganic or organic

species in many cases under controlled conditions [57, 58]. However, top-down strategy is also

effective for the preparation of 2D particles [59].
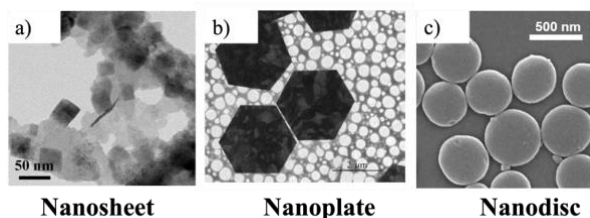
Figure 1.8. Typical 2D-shaped particles [54,55, 56]
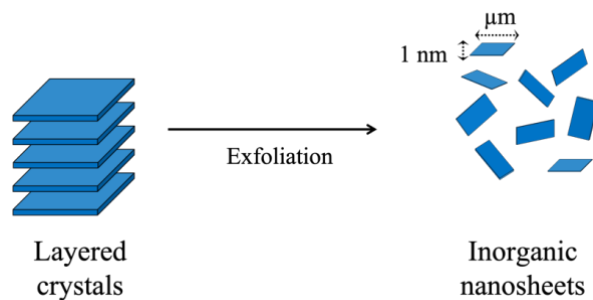
Figure 1.9. Schematic process for inorganic nanosheet preparation by exfoliation of layered crystals

Inorganic nanosheets are typical examples of 2D particles prepared by the top-down strategy [60].   This type of 2D particles is obtained by exfoliation of layered crystals as shown in Figure 1.9.   The exfoliated nanosheets distinguished from other 2D particles by their high shape anisotropy because of their thickness of around 1-nm and lateral length of up to micrometers. Table 1 listed examples of nanosheets obtained from inorganic layered crystals.   Various oxides, hydroxides, chalcogenides, nitrides, and simple substances are included.   These nanosheets can be stabilized in solvents as colloidal particles if their surfaces have affinity to the solvents.

Table 1 Example of nanosheets obtained from inorganic layered crystals [60]

Substance group	Typical examples		
Oxides	$Cs_{0.7}Ti_{1.825}O_4$	$K_{0.45}MnO_2$	$KCa_2Nb_3O_{10}$
Hydroxides	$[Mg_{1-x}Al_x(OH)_2][(NO_3)x \cdot nH_2O]$		
	$[Li_{1/3}Al_{2/3}(OH)_2][Cl_{1/3} \cdot nH_2O]$		
Chalcogenides	MoS_2	WS_2	Ta_2NiS_5
Nitride	BN		
Others	*Clay minerals (montmorillonite, hectorite)*		

1.3.2. Principles of structure construction from 2D particles

Colloidal 2D particles can be assembled into more diverse structures than 1D particles due to their 2D shape. A typical example is the manner of interparticle connection. Although 1D particles can be assembled through end-end and side-side connections, 2D particles can be organized through edge-edge, edge-face, and face-face interactions [61, 62, 63]. Although dimensional transformation of 1D particles to 2D and 3D assemblies hardly gives well-defined structures, 2D particles can be converted to both of structurally well-defined 1D and 3D assemblies [64, 65]. Moreover, interparticle spaces between the 2D particles can be used for confining other molecules and nanoparticles with certain arrangement [66]; however, 1D particles do not give such nanospaces between them.

Colloidal 2D particles can be self-assembled and/or assembled with external forces, like 1D particles. Interactions between the particles are anisotropic as those between 1D particles. However, the biaxial nature of 2D particles gives more complicated particle-particle interactions than 1D particles. However, owing to the flexibility of the 2D morphologies, the 2D particles are often scrolled, folded, and deformed as shown in Figure 10, which make regularly ordered particle assemblies rather

difficult. This induce the assemblies of 2D particles tend to be small-sized and do not have highly-ordered structures as shown in Figure1.10. For these reasons, 2D particles have often been assembled into solid films or monoliths [63, 68]. In the former case, the 2D shape is simply expended to a macroscopic scale on the surface of appropriate substrates. In the latter, the 2D particles are randomly assembled with extra species to form disordered 3D structures. As results, large-scale regularly ordered assemblies of colloidal 2D particles has not been well developed at present, although superstructures in hierarchical manners have been reported [67].
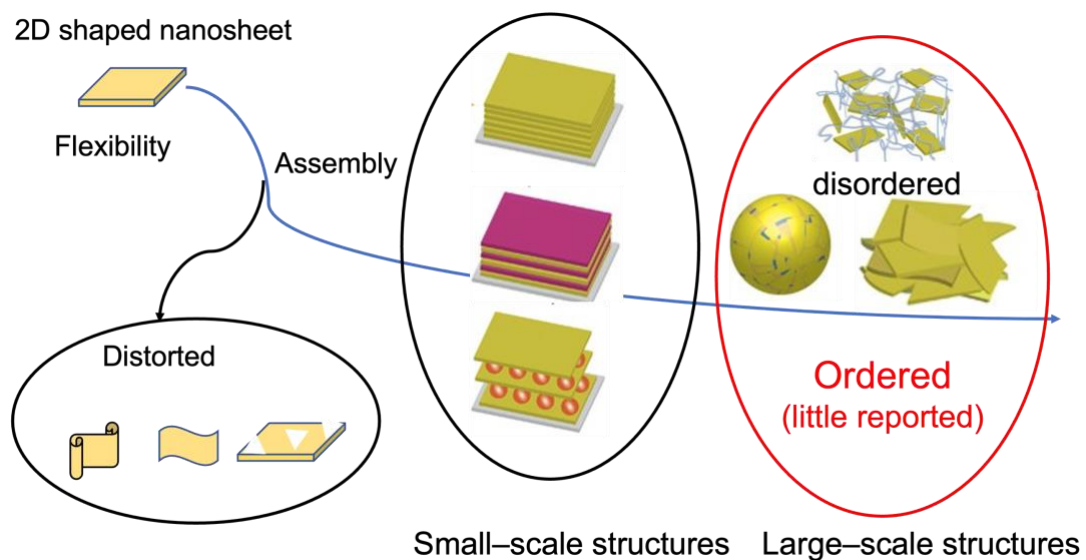
Figure 1.10. Schematic representation of 2D particle assemblies status. The 2D shaped nanosheets have been assembled into well-ordered small-scale structures and disordered large-scale structures, however, the ordered large-scale structures have been rarely reported [63]

1.3.3. Inorganic nanosheets and their assemblies

Colloids of inorganic nanosheets obtained by exfoliation of layered crystals have attracted attentions recently as structured colloids [69, 70, 71], where the particles are dispersed with a certain manner. These nanosheets are distinguished from other 2D particles by their extreme thickness which leads very high shape anisotropy. Typical colloidal structures of inorganic nanosheets are orientational ordering of the particles. Because of their high shape anisotropy, nanosheets require large volumes for free rotation. Thus, their free rotation is prohibited in the colloids with high nanosheet concentration, leading to entropic loss of the system. When a part of nanosheets is orientationally ordered in such a concentrated colloid, ordering particles obtain large translational entropy and the rest particles recover the freedom of rotation to maximize the entropy of the system. This process is schematically shown in Figure 1.11 [19].
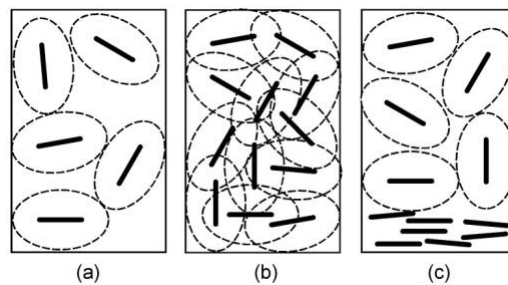
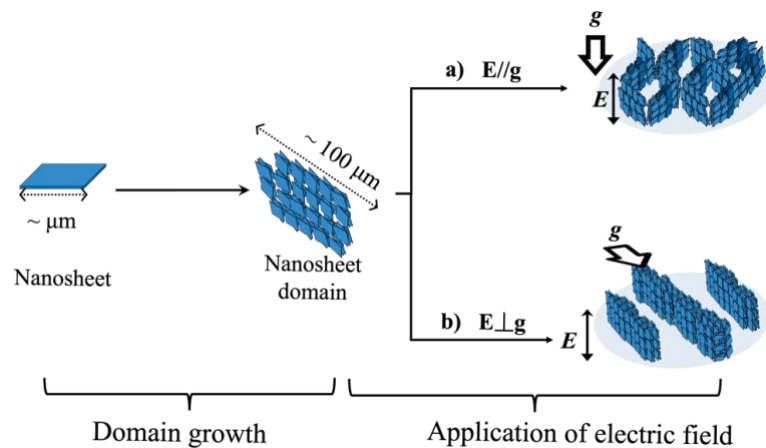*Figure 1.11. Schematic representation of isotropic-nematic transition in an anisotropic colloid. (a) particles are randomly dispersed to form isotropic phase at a low concentration, (b) overlap of excluded volume (represented by ellipse surrounded with dash line) of particles at high concentration, (c) When a part of particles are orientationally ordered, excluded volume of the residual particle is recovered [19]*

16

The evolution of nanosheet ordering in their colloids is a kind of phase separation [69, 70, 71]. The ordered nanosheets are assembled with themselves to form domains and separated from isotropically dispersed nanosheets in the colloids.   This is an example of hierarchical organization of colloidal nanosheets. The domains of ordered nanosheets are recognized as a structure of higher hierarchy.   Also, the domains can be manipulated as secondary building blocks of the colloid by external force [24, 72].

A typical example of the hierarchical structures in the nanosheet colloids is the formation of macroscopic structures in the colloids of hexaniobate nanosheets [24].   The strategy for the hierarchical organization is the use of a two-stage process, as schematically shown in Figure 1.12.   The first stage is controlled growth of nanosheet domains called tactoids by assembly of nanosheets. This is key step to macroscopic structures because the growth tactoids have the dimensions of sub-mm length, being much larger than individual nanosheets at μm length, and act as secondary building blocks of the final structures.   The tactoids are further assembled into macroscopic higher-order structures by application of an AC electric field as the second stage.   The final structures have characteristic lengths of sub-mm to mm reflecting the tactoid size.   In this stage, relative directions of the electric field and gravity determine the final structure. A net-like texture forms when the electric field and gravitational forces are applied from the same

17

direction. The tactoids grown prior to the AC voltage application work as the secondary

building blocks of the final structures under the electric field.

In contrast, a stripe texture is obtained when the electric field is applied in the

direction perpendicular to gravity. This texture reflects unidirectional nanosheet

alignment. Each stripe has a characteristic length of sub-mm in width and mm in length.

Direction of the stripe is the same as that of gravity.   Because the 2D shape of nanosheets

requires regulation from two orthogonal directions for uniquely determining their

alignment.   The electric field applied to the sample sets the direction of nanosheets

perpendicular to the cell surface, and the in-plane direction with respect to the cell surface

is determined.

Figure 1.12. Schematic representation of hierarchical assembly of inorganic nanosheet colloid with a two-stage process including domain growth (left) and application of electric field (right) from direction (a) parallel to gravity and (b) perpendicular to gravity. The arrows indicate the direction of electric field (E) and gravity (g), respectively.

1.4. Purpose of the present research

Based on the above backgrounds, the author examined preparation of novel hierarchical assemblies from colloidal anisotropic particles with 1D and 2D shapes. CNC nanorods and inorganic nanosheets were employed as typical 1D and 2D particles, respectively. For the CNC rods, although numerous hierarchical structures have already been assembled by many researchers, compartmentalization of the CNC assemblies have not been investigated well. However, compartmentalized CNC assemblies are important easily handleable building blocks of CNC-based multiscale materials. Hence, the author tried to compartmentalize CNC nanorods with a choice of core-shell particle fabrications. These core-shell particles are small-scale compartmentalized structures. They can be easily handled and incorporated into integrated systems for high-ordered structure preparations.   On the other hand, for 2D particles represented by the inorganic nanosheets, their organization into hierarchical structures has relatively been unexplored. Although the hierarchical organization with the aid of an electric field has been reported as described in Section 1.3.3, reproducibility and quantitative evaluation of the structure have not been clarified.   Thus, the author tried to quantitative evaluation and reproducible assembly of unidirectionally aligned structures of colloidal inorganic nanosheets. These macroscopic unidirectional structures have high regular alignments to mm level. They are breakthroughs for both large-scale

regularly ordered assembly and colloidal state assembly of 2D nanosheet structures.

References

1. A. D. McNaught and A. Wilkinson. Compendium of Chemical Terminology, 2nd ed. (the "Gold Book"). Blackwell Scientific Publications, 1997.

2. A. Henglein. Small-particle research: physicochemical properties of extremely small colloidal metal and semiconductor particles. *Chem. Rev.*, 1989, **8**, 1861-1873.

3. Y. Cui, M. T. Bjork, J. A. Liddle, C. Sonnichsen, B. Boussert, A. P. Alivisatos. Integration of colloidal nanocrystals into lithographically patterned devices. *Nano Lett.*, 2004, **4**, 1093-1098.

4. Y. Lvov, K. Ariga, M. Onda, I. Ichinose, T. Kunitake. Alternate assembly of ordered multilayers of SiO2 and other nanoparticles and polyions. *Langmuir*, 1997, **13**, 6195-6203.

5. K. L. Young, M. L. Personick, M. Engel, P. F. Damasceno, S. N. Barnaby, R. Bleher, T. Li, S. C. Glotzer, B. Lee, C. A. Mirkin. A directional entropic force approach to assemble anisotropic nanoparticles into superlattices. *Angew. Chem. Int. Ed.*, 2013, **52**, 13980-13984.

6. Y. Lvov, K. Ariga, I. Ichinose, T. Kunitake. Assembly of multicomponent protein films by means of electrostatic layer-by-layer adsorption. *J. Am. Chem. Soc.*, 1995, **117**, 6117-6123.

7. J. Bernasconi, S. Strassler, H. R. Zeller. Van der Waals contribution to the surface and anchoring energies of nematic liquid crystals. *Phys. Rev. A*, 1980, **22**, 276-281.

8. K. L. Young, M. L. Personick, M. Engel, P. F. Damasceno, S. N. Barnaby, R. Bleher, T. Li, S. C. Glotzer, B. Lee, C. A. Mirkin. A directional entropic force approach to

assemble anisotropic nanoparticles into superlattices. *Angew. Chem. Int. Ed.*, 2013, **52**, 13980-13984.

9. E. J. W. Verwey. Theory of the stability of lyophobic colloids. *J. Phys. Chem.*, 1947, **51**, 631-636.

10. B. V. Derjaguin, L. D. Landau. Theory of the stability of strongly charged lyophobic sols and of adhesion of strongly charged particles in solutions of electrolytes. *Acta physiochem.*, 1941, **14**, 633-662.

11. W. Fan, M. Chen, S. Yang, L. Wu. Centrifugation-assisted assembly of colloidal silica into crack-free and transferrable films with tunable crystalline structures. *Sci. Rep.*, 2015, **5**, 12100.

12. F. Xu, P. Zhang, A. Navrotsky, Z. -Y. Yuan, T. –Z. Ren, M. Halasa, B. -L. Su. Hierarchically assembled porous ZnO nanoparticles: synthesis, surface energy, and photocatalytic activity. *Chem. Mater.*, 2007, **19**, 5680-5696.

13. P. N. Pusey, W. Van Megen. Phase behavior of concentrated suspension of nearly hard colloidal spheres. *Nature*, 1986, **320**, 340-342.

14. C. T. Desire, A. Lotierzo, R. D. Arrua, E. F. Hilder, S. A. F. Bon. Robust open cellular porous polymer monoliths made from cured colloidal gels of latex particles. *Green Chem.*, 2018, **20**, 2499-2511.

15. P. Pieranski. Colloidal crystals. *Contemp. Phys.*, 1983, **24**, 25-73.

16. S. Y. Zhang, M. D. Regulacio, M. Y. Han. Self-assembly of colloidal one-dimensional nanocrystals. *Chem. Soc. Rev.*, 2014, **43**, 2301-2323.

17. G. H. Jeong, S. P. Sasikala, T. Yun, G. Y. Lee, W. J. Lee, S. O. Kim. Nanoscale assembly of 2D materials for energy and environmental applications. *Adv. Mater.*, 2020, **32**, 1907006.

18. A. Maestro, E. Guzman. Colloids at fluid interfaces. *Processes*, 2019, **7**, 942.

19. L. Onsager. The effect of shape on the interaction of colloidal particles. *Ann. N. Y. Acad. Sci.*, 1949, **51**, 627-659.

20. S. Shabaniverki, J. J. Juarez. Directed assembly of particles for additive manufacturing of particle polymer composites. *Micromachines*, 2021, **12**, 935.

21. Y. Brasse, V. Gupta, H. C. T. Schollbach, M. Karg, T. A. F. Konig, A. Fery. Mechanotunable plasmonic properties of colloidal assemblies. *Adv. Mater. Interfaces*, 2020, **7**, 1901678.

22. J. Wu, Y. Xu, X. Ma, H. Tian. End-to-end assembly and disassembly of gold nanorods based on photo-responsive host-guest interaction. *Chem. Commun.*, 2017, **53**, 4577-4580.

23. Controlled side-by-side assembly of gold nanorods and dye molecules into polymer-rapped SERRS-active clusters. *Chem. Commun.*, 2011, **47**, 3757-3759.

24. T. Nakato, Y. Nono, E. Mouri, M. Nakata. Panoscopic organization of anisotropic colloidal structures from photofunctional inorganic nanosheet liquid crystals. *Phys. Chem. Chem. Phys.*, 2014, **16**, 955-962.

25. G. Lazzara, G. Cavallaro, A. Panchal, R. Fakhrulin, A. Stavitskaya, V. Vinokurov, Y. Lvov. An assembly of organic-inorganic composites using halloysite clay nanotubes. *Curr. Opin. Colloid Interface Sci.*, 2018, **35**, 42-50.

26. D. V. Talapin, C. T. Black, C. R. Kagan, E. V. Shevchenko, A. Afzali, C. B. Murray. Alignment, electronic properties, doping, and on-chip growth of colloidal PbSe nanowires. *J. Phys. Chem. C*, 2007, **111**, 13244-13249.

27. B. Sun, H. Sirringhaus. Solution-processed zinc oxide field-effect transistors based on self-assembly of colloidal nanorods. *Nano lett.*, 2005, **5**, 2408-2413.

28. M. R. Badrossamay, H. A. McIlwee, J. A. Goss, K. K. Parker. Nanofiber assembly by rotary Jet-spinning. *Nano lett.*, 2010, **10**, 2257-2261.

29. J. Zimmermann, G. R. J. Artus, S. Seeger. Long term studies on the chemical stability of a superhydrophobic silicone nanofilament coating. *Appl. Surf. Sci.*, 2007, 253, 5972-5979.

30. Y. Huang, X. Duan, Q. Wei, X. M. Lieber. Directed assembly of one-dimensional nanostructures into functional networks. *Science*, 2001, **291**, 630-633.

31. S. A. Maier, M. L. Brongersma, P. G. Kik, S. Meltzer, A. A. G. Requicha, H. A. Atwater. Plasmonics – a route to nanoscale optical devices. *Adv. Mater.*, 2001, **13**, 1501-1505.

32. D. A. Schultz. Plasmon resonant particles for biological detection. *Curr. Opin. Biotechnol.*, 2003, **14**, 13-22.

33. A. G. Tkachenko, H. Xie, D. Coleman, W. Glomm, J. ryan, M. F. Anderson, S. Franzen, D. L. Feldheim. Multifunctional gold nanoparticle-peptide complexes for nuclear targeting. *J. Am. Chem. Soc.*, 2003, **125**, 4700-4701.

34. P. R. Sajanlal, T. S. Sreeprasad, A. K. Samal, T. Pradeep. Anisotropic nanomaterials: structure, assembly, and functions. *Nano Rev.*, 2011, **2**, 5883.

35. W. Kim, E. Park, S. Jeon. Performance enhancement of a quartz tuning fork sensor using a cellulose nanocrystal-reinforced nanoporous polymer fiber. *Sensors*, 2020, **20**, 437.

36. D. Trache, M. H. Hussin, M. K. M. Haafiz, V. K. Thakur. Recent progress in cellulose nanocrystals: sources and production. *Nanoscale*, 2017, **9**, 1763-1786.

37. J. George, SN Sabapathi. Cellulose nanocrystals: synthesis, functional properties, and applications. *Nanotechnol. Sci. Appl.*, 2015, **8**, 45-54.

38. Y. Habibi, L. A. Lucia, O. J. Rojas. Cellulose nanocrystals: self-Assembly, and applications. *Chem. Rev.,* 2010, **110,** 3479-3500.

39. J. M. Buffa, U. Casodo, V. Mucci, M. I. Aranguren. Cellulose nanocrystals in aqueous suspensions: rheology of lyotropic chiral liquid crystals. *Cellulose*, 2019, **26**, 2317-2332.

40. Y. Ogawa. Electron microdiffraction reals the nanoscale twist geometry of cellulose nanocrystals. *Nanoscale*, 2019, **11**, 21767-21774.

41. J. Majoinen, E. Kontturi, O. Ikkala, D. G. Gray. SEM imaging of chiral nematic films cast from cellulose nanocrystal suspensions. *Cellulose*, 2012, **19**, 1599–1605.

42. A. Tran, C. E. Boott, M. J. Maclachlan. Understanding the self-Assembly of cellulose nanocrystals-Toward chiral photonic materials. *Adv. Mater.*, 2020, **32**, 1905876.

43. Y. P. Zhang, V. P. Chodavarapu, A. G. Kirk, M. P. Andrews. Structured color humidity indicator from reversible pitch tuning in self-assembled nanocrystalline cellulose films. *Sens. Actuators B Chem.*, 2013, **176**, 692-697.

44. M. S. Islam, L. Chen, J. Sisler, K. C. Tam. Cellulose nanocrystal (CNC) -inorganic hybrid systems: synthesis, properties and applications. *J. Mater. Chem. B*, 2018, **6**, 864-883.

45. S. Wang, A. Lu, L. Zhang. Recent advances in regenerated cellulose materials. *Prog. Polym. Sci.*, 2016, **53**, 169-206.

46. A. Khan, R. A. Khan, S. Salmieri, C. L. Tien, B. Riedl, J. Bouchard, G. Chauve, V. Tan, M. R. Kamal, M. Lacroix. Mechanical and barrier properties of nanocrystalline cellulose reinforced chitosan based nanocomposite films. *Carbohydr. Polym.*, 2012, **90**, 1601-1608.

47. N. Lin, A. Dufresne. Physical and/or chemical compatibilization of extruded

cellulose nanocrystal reinforced polystyrene nanocomposites. *Macromolecules*, 2013, **46**, 5570-5583.

48. K. B. Azouz, E. C. Ramires, W. V. D. Fonteyne, N. EI Kissi, A. Dufresne. Simply method for the melt extrusion of cellulose nanocrystal reinforced hydrophobic polymer. *ACS Macro. Lett.*, 2012, **1**, 236-240.

49. R. Baedet, N. Belgacem, J. Bras. Flexibility and color monitoring of cellulose nanocrystal iridescent solid films using anionic or neutral polymers. *ACS Appl. Mater. Interfaces*, 2015, **7**, 4010-4018.

50. K. Yao, Q. Meng, V. Bulone, Q. Zhou. Flexible and responsive chiral nematic cellulose nanocrystal/poly (ethylene glycol) composite films with uniform and tunable structural color. *Adv. Mater.*, 2017, **29**, 17023.

51. Z. Zhang, M. Cheng, M. S. Gabriel, A. A. T. Neto, J. da S. Bernardes, R. Berry, K. C. Tam. Polymeric hollow microcapsules (PHM) via cellulose nanocrystal stabilized Pickering emulsion polymerization. J. Colloid Interface Sci., 2019, 555, 489-497.

52. R. M. Park, B. F. Petesic, G. Guidetti, G. Kamita, G. Consani, C. Abell, S. Vignolini. Hierarchical self-assebly of cellulose nanocrystals in a confined geometry. *ACS Nano*, 2016, **10**, 8443-8449.

53. Z. Hu, T. Patten, R. Pelton, E. D. Cranston. Synergistic stabilization of emulsion and emulsion gels with water-soluble polymers and cellulose nanocrystals. *ACS Sustainable Chem. Eng.*, 2015, **3**, 1023-1031.

54. J. Hao, W. Li, X. Zuo, D. Zheng, X. Liang, Y. Qiang, B. Tan, B. Xiang, X. Zou. Facile electrochemical phosphatization of Mn_3O_4 nanosheet arrays for supercapacitor with enhanced performance. *J. Mater. Sci.*, 2019, **54**, 625-637.

55. C. Wang, C. Kan, J. Zhu, X. Zeng, X. Wang, H. Li, D. Shi. Synthesis of high-yield

gold nanoplates: fast growth assistant with binary surfactants. *J. Nanomater.*, 2010, **2010**, 969030.

56. V. Giglio, S. V. Aramburu, L. Travaglini, F. Fiorini, P. H. Seeberger, L. Maggini, L. D. Cola. Reshaping silica particles: mesoporous nanodiscs for biomodal delivery and improved cellular uptake. *Chem. Eng. Sci.*, 2018, **340**, 148-154.

57. Y. Chen, Z. Fan, Z. Zhang, W. Niu, C. Li, N. Yang, B. Chen, H. Zhang. Two-dimensional metal nanomaterials: synthesis, properties, and applications. *Chem. Rev.,* 2018, **118**, 6409-6455.

58. I. Vlassiouk, M. Regmi, P. Fulvio, S. Dai, P. Datskos, G. Eres, S. Smirnov. Role of hydrogen in chemical vapor deposition growth of large-crystal graphene. *ACS Nano*, 2011, **5**, 6069-6076.

59. Z. Zhang, A. Fraser, S. Ye, G. Merle, J. Barralet. Top-down bottom-up graphene synthesis. *Nano Futures*, 2019, **3**, 042003.

60. T. Nakato, J. Kawamata, S. Takagi. Inorganic nanosheets and nanosheet-based materials. *Springer*, Tokyo, 2017.

61. X. D. Zhang, Q. H. Liu, L. J. Meng, H. Wang, W. T. Bi, Y. H. Peng, T. Yao, S. Q. Wei, Y. Xie. In-plane coassembly route to atomically thick inorganic-organic hybrid nanosheets. *ACS Nano*, 2013, **7**, 1682-1688.

62. M. J. Liu, Y. Ishida, Y. Ebina, T. Sasaki, T. Hikima, M. Takata, T. Aida. An anisotropic hydrogel with electrostatic repulsion between cofacially aligned nanosheers. *Nature*, 2015, **517**, 68-72.

63. M. Osada, T. Sasaki. Nanosheet architectonics: a hierarchically structured assembly for tailored fusion materials. Polym. J., 2015, 47, 89-98.

64. Z. C. Lai, Y. Chen, C. L. Tan, X. Zhang, H. Zhang. Self-assembly of two-dimensional

nanosheets into one-dimensional nanostructures. *Chem.*, 2016, **1**, 59-77.

65. J. L. Zou, F. Kim. Diffusion driven layer-by-layer assembly of graphene oxdie nanosheets into porous three-dimensional macrostructures. *Nat. Commun.*, 2014, **5**, 5254.

66. T. Shichi, K. Takagi. Clay minerals as photochemical reaction fields. *J. Photochem. Photobiol. C*, 2000, **1**, 113-130.

67. Q. C. Jia, X. Y. Huang, G. Y. Wang, J. C. Diao, P. K. Jiang. MoS_2 nanosheet superstructures based polymer composite for high-dielectric and electrical energy storage applications. *J. Phys. Chem. C*, 2016, **120**, 10206 -10214.

68. S. S. Tong, X. Zhou, C. H. Zhou, Y. Y. Li, W. J. Li, W. H. Zhou, Q. Jia. A strategy to decorate porous polymer monoliths with graphene oxide and graphene nanosheets. *Analyst*, 2013, **138**, 1549-1557.

69. N. Miyamoto, T. Nakato. Liquid crystalline nanosheet colloids with controlled particle size obtained by exfoliating single crystal of layered niobate $K_4Nb_6O_{17}$. *J. Phys. Chem. B*, 2004, **108**, 6152-6159.

70. N. Miyamoto, T. Nakato. Liquid crystalline inorganic nanosheet colloids derived from layered materials. *Isr. J. Chem.*, 2012, **52**, 881-894.

71. T. Nakato, N. Miyamoto. Liquid crystalline behavior and related properties of colloidal systems of inorganic oxide nanosheets. *Materials*, 2009, 2, 1734-1761.

72. Y. Nono, E. Mouri, M. Nakata, T. Nakato. Flow-induced assembly of colloidal liquid crystalline nanosheets toward unidirectional macroscopic structures. *J. Nanosci. Nanotechno.*, 2016, **16**, 2967-2974.

73. Y. Xie, Y. Li, G. Wei, Q. Liu, H. Mundoor, Z. Chen, I. I. Smalyukh. Liquid crystal self-assembly of upconversion nanorods enriched by depletion forces for

mesostructured materials preparation. *Nanoscale*, 2018, **10**, 4218-4227.

74. M. Osada, T. Sasaki, K. Ono, Y. Kotani, S. Ueda, K. Kobayashi. Orbital reconstruction and interface ferromagnetism in self-assembled nanosheet superlattices. *ACS Nano*, 2011, **5**, 6871-6879.

75. Z. Guo, X. Feng, X. Li, X. Zhang, X. Peng, H. Song, J. Fu, K. Ding, X. Huang, B. Gao. Nitrogen-doped carbon nanosheets encapsulated in situ generated sulfur enable high capacity and superior rate cathode for Li-S batteries. *Front. Chem.*, 2018, **6**, 429.

76. S. Ida, A. K. Thapa, Y. Hidaka, Y. Okamoto, M. Matsuka, H. Hagiwara, T. Ishihara. Manganese oxide with a card-house-like structure reassembled from nanosheets for rechargeable Li-air battery. *J. Power Sources*, 2012, **203**, 159-164.

77. S. Y. Zhang, M. D. Regulacio, M. Y. Han. Self-assembly of colloidal one-dimensional nanocrystals. *Chem. Soc. Rev.*, 2014, **43**, 2301-2323.

78. B. Zhu, R. Merindol, A. J. Benitez, B. Wang, A. Walther. Supermolecular engineering of hierarchically self-assembled, bioinspired, cholesteric nanocomposites formed by cellulose nanocrystals and polymers. *ACS Appl. Mater. Interface*, 2016, **8**, 11031-11040.

79. W. Kim, E. Park, S. Jeon. Performance enhancement of a quartz tuning fork sensor using a cellulose nanocrystal-reinforced polymer fiber. *Sensor*, 2020, **20**, 437.

Chapter 2. Fabrication of CNC-polymer core-shell particles

with CNC cores

Chapter 2. Fabrication of CNC-polymer core-shell particles with CNC cores

2.1. Introduction

Cellulose nanocrystals (CNCs) are anisotropic, rod-shaped nanoparticles [1, 2, 3]. CNCs are regarded as one of the most promising sustainable and nontoxic materials, having versatile, attractive characteristics such as high mechanical strength, high gas barrier, and unique optical properties [4, 5, 6]. CNCs form stable aqueous colloids and are arranged in a helical manner [3, 7], which is responsible for the versatile properties of CNCs. Because the aqueous CNC colloids are generally viscous because of rich hydrogen bonding between the rods [8]. Thus, development of compartmentalization of CNC colloids is an important topic for their application as practical materials.

Incorporating CNCs with general polymers is a promising strategy of compartmentalizing the colloidal CNC particles. Especially, particulate composite fabrication of CNCs with polymers would be worth developed. One of the reasons is that the surface of CNCs is so hydrophilic that CNCs cannot be easily dispersed in a non-polar matrix simply by mixing [9, 10]. Thus, stable composite fabrication using polymers is a practical way of imparting amphiphilic properties to CNCs [11, 12]. In addition, the

particulate composite can be used as a secondary building block to fabricate higher-order

materials with more sophisticated architecture, an application that cannot be achieved

with film-based CNC materials.

In fact, confinement of CNCs in particles have been challenged by some groups.

They fabricated core-shell particles with CNC core by utilizing microfluidic

emulsification [13, 14].   Wang et al. also reported the synthesis of core-shell particles

with CNC cores by emulsion polymerization, which yielded particles with 30–200 μm

diameters [15].   On the other hand, Jativa et al. also reported CNC capsules, in which

CNCs are in the shell of a core-shell particle [16].   However, no previous studies have

reported a particulate composite fabrication method that can create core-shell particles

that contain CNCs either in the core or the shell; developing a widely applicable method

is a challenge.   To widen the selection of possible counterpart components, the

fabrication method should be simply, with few restrictions.

Based on these backgrounds, the authors propose a facile and tunable fabrication

method of core-shell particles of CNCs and water-soluble polymers.   The authors

employed the self-organized precipitation (SORP) method proposed by Yabu [17, 18, 19].

Unlike other methods such as dispersion polymerization or emulsion polymerization [20,

21, 22, 23], the SORP method does not require strict polymerization control or additional

surfactant. The SORP method is known to be a facile method for preparing particles composed of two components. In usually involves two solutes and two miscible solvents (one solvent is good at dissolving solutes, while the other is poor). When the good solvent is evaporated, the solubility of the solutes decreases, causing core-shell particles to form. The particle architecture, i.e., the component location, is controlled by the difference in affinity between the two solutes and the poor solvent. The solute with lower affinity to the poor solvent is firstly deposited as cores, and the other solute deposited over the cores to form shells. In this chapter, the author described the fabrication of CNC-polymer core-shell particles with CNC cores. Polyethylene glycol was adopted as the shell material.

2.2. Experimental

In the experiment, CNCs and polyethylene glycol with average molecular weight of 2000 (PEG2000) were used as two solutes, and water and ethylene glycol (EG) were used as two solvents. In the system, water is good solvent for both CNC and PEG2000, and EG is poor solvent comparing to water. Meanwhile, EG has higher boiling point than water. We choose PEG as the polymer component because PEG has been widely applied in biomedical materials because of its non-toxicity and biodegradability,

characteristics that could make the combination of CNCs and PEG as s sustainable

material.   Figure 2.1 shows a schematic representation of the SORP method applied to

the CNC-PEG2000 solute in the water-EG system.   First, CNCs and PEG2000 are

dissolved in water (Figure 2.1a), and EG is added to the solution (Figure 2.1b). Water

then evaporates, while EG remains unevaporated (Figure 2.1c).   In this process, CNCs

and PEG2000 tend to deposit because of their decreased solubility in EG.   Owing to the

higher solubility of PEG2000 in EG than CNC solubility in EG, PEG2000 has higher

affinity to EG than that of CNC-EG.   With such a fact, the formation of CNC-core

particles can be expected since the PEG2000-EG affinity is greater than CNC-EG, where

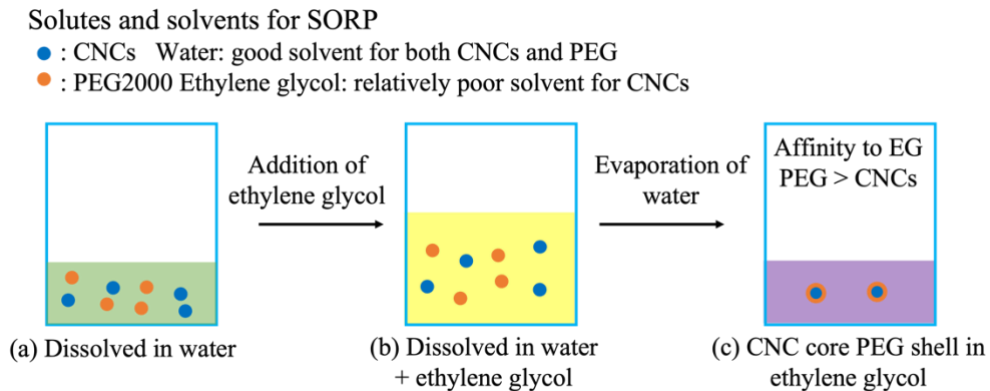PEG2000 will form a shell around the CNC core.

Figure 2.1. Schematic process for fabrication of CNC-core particles via SORP method [24]

2.2.1. Materials

In the experimental, CNCs having a length of around 40-100 nm and width of 2-

5 nm were purchased from CelluForce, Canada. CNC has sulfonic acid groups with

sulfate content of ca. 250 mmol kg $^{-1}$. PEG2000 were purchased from Wako Chemical Industry, Japan, and it has molecular weight ranges between 1,800-2,200 as claimed by the supplier. EG is also purchased from Wako Chemical Industry, Japan. The water used in the experiment is Mill-Q water.

2.2.2. Fabrication of CNC-core Particles

The sample preparation procedure is represented in Figure 2.1. CNCs and PEG were separately dispersed in Mill-Q water completely to a concentration of 8 g L^{-1}. For the preparation of the CNC/PEG sample, the CNC dispersion was mixed with the PEG dispersion and water to prepare 4mL of 2g L^{-1} of CNCs and PEG2000. The same volume (4 mL) of ethylene glycol was gradually added to form an aqueous mixture. The solution was stirred form 24 hours to prepare a mixture of CNCs (1 g L^{-1}) and PEG2000 (1 g L^{-1}) in the water/ethylene glycol solvent mixture.

For obtaining core-shell particles from the system, the mixtures were heated at 45 ℃ to evaporate to half the volume in order to remove the water and obtain the EG solution. The evaporation of ca. 2 mL of water out of 4 mL mixture solution takes three days. As discussed in the following section, we could not observe the particle formation clearly by the optical microscope, thus we took small amounts of the dispersions and kept in a 40 ℃ vacuum oven for two days to dry completely.

To identify the core-shell components, we introduced rhodamine 6G (R6G) as the fluorescent probe and prepared samples of CNC/PEG2000 containing R6G with the same procedure as the above.   R6G was added to the CNC/PEG aqueous mixture to a concentration of 2.46×10^{-5} mol L^{-1} before EG addition.   The final concentration of R6G in the water/EG mixture solvents was 1.23×10^{-5} mol L^{-1}. The dried CNC/PEG2000/R6G particles were obtained with same procedure as the above.

2.2.3. Characterization

The CNC/PEG2000 samples without R6G in different stages were observed with optical microscope (Olympus BX-51, Tokyo, Japan). To confirm the selective adsorption of R6G, samples of various solvent combinations with solute concentration of 1g L^{-1} and R6G concentration of 1.23×10^{-5} mol L^{-1} are measured with a UV-vis spectrophotometer UV-2600 (Shimadzu, Japan) and a spectrofluorometer FP-8500 (Jasco, Japan). The component identification in R6G labelled sample was observed with fluorescent optical microscope equipped with a Bx2-FL-1 fluorescent unit using an Olympus U-MSWB-3 mirror.

To confirm the 3-dimentional morphologies of the fabricated particles, the samples were dropped on the mica and dried in 40 ℃ vacuum oven. The dried samples on the mica were observed with the Atomic Force microscope (AFM). AFM images were

taken on a Nanonavi IIs station and nanocute (SII Nanotechnology, Tokyo, Japan) in the

dynamic force mode with a cantilever (PRC-DF40P, SII Nanotechnology, Tokyo, Japan).

2.3. Results and discussion

The appearance of CNC/PEG2000 in the process of SORP were presented in

Figure 2.2. The CNC/PEG2000 in water/EG mixture solvent was transparent as shown in

Figure 2.2a. Its optical microscope image illustrated in Figure 2.2c also indicated no

particles.　When the water was evaporated, CNC/PEG2000 left in EG were still

transparent as shown in Figure 2.2b. In its corresponding optical microscope image as

illustrated in Figure 2.2d, no particles were observed.
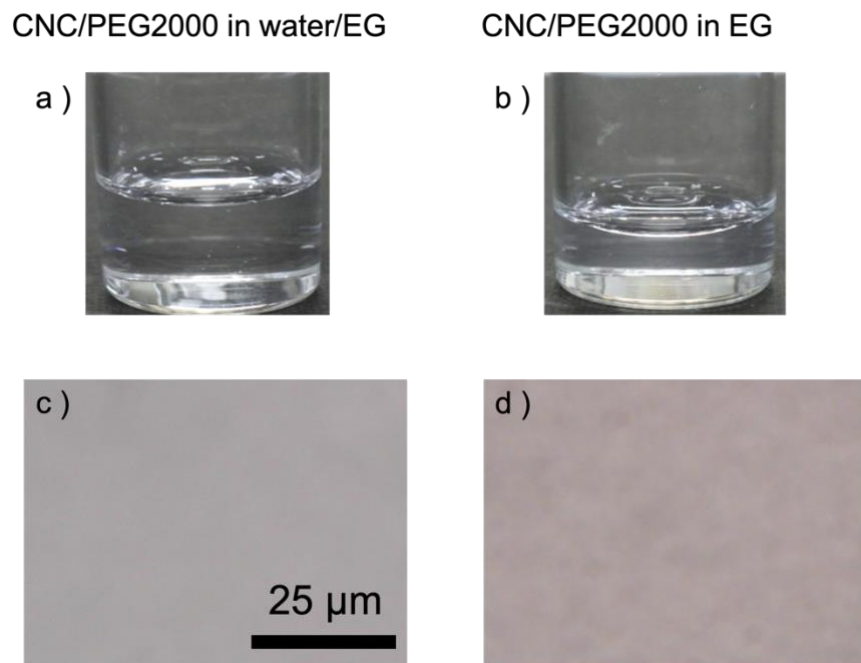
Figure 2.2. Appearance of CNC/PEG2000 in water/EG (a), EG (b) observed with naked eye and CNC/PEG2000 in water/EG (c), EG (d) observed with optical microscope [24]

In this case, a small amount of solution was dried in vacuum oven and observed

with optical microscope to confirm particle formations. As illustrated in Figure 2.3, numerous monodisperse spherical particles around 1 μ m with clear core-shell contours were observed. These particles had brighter shell than the cores, which were dark gray.
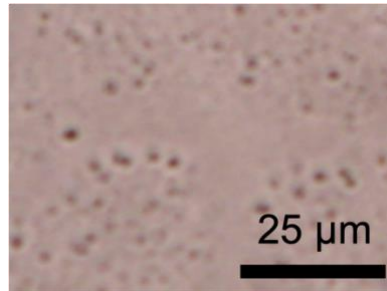
Figure 2.3. Optical microscope image of dried CNC/PEG2000 [24]

Independently, we checked the dispersibility of the two components, PEG2000 and CNC, in EG as illustrated in Figure 2.4. PEG2000 was fully dispersed in EG (a) and CNC was partly dispersed in EG (b). Based on the higher solubility of PEG2000 in Figure 2.4, affinity of PEG2000 to EG would be higher than that of CNC. Thus, CNC core formation is more reasonable to occur if the particles are obtained with this system by SORP.
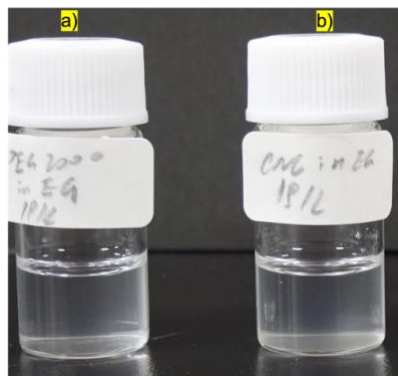
Figure 2.4. Solubility appearance of 1 g L $^{-1}$ PEG2000 (a) and CNC (b) in ethylene glycol

We confirmed the core-shell particle formation by the observation at dried state, but we do not have any information about the component of which the core and shell parts are composed. In order to characterize the component, either CNC and PEG2000, we introduced cationic dye R6G, which is expected to be adsorbed to the anionic surface of CNC.
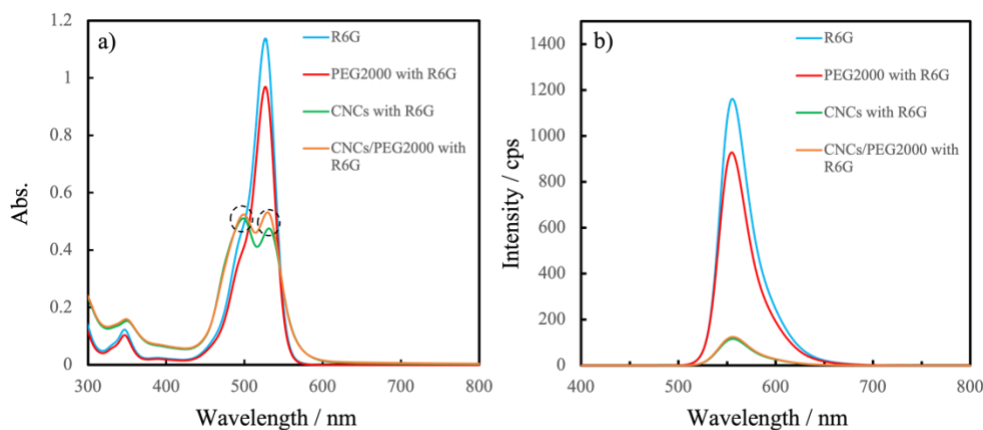

Figure 2.5. UV-vis spectra (a) and fluorescent spectra (b) of various combinations of samples in water containing 1g L $^{-1}$ solutes and 1.23 x 10 $^{-5}$ mol L $^{-1}$, the excitation wavelength in fluorescent measurement is 347 nm [24].

In order to confirm the selective adsorption of R6G on which component, the UV-vis spectra and fluorescent spectra of various samples with water as solvent were illustrated in Figure 2.5. The solute concentration was 1 g L $^{-1}$ and R6G concentration was 1.23 x 10^{-5} mol L $^{-1}$. The UV-vis spectra in Figure 2.5a indicated that PEG2000 with R6G had same adsorption wavelength with R6G only while CNC with R6G and CNC/PEG2000 with R6G had two different adsorption wavelengths different from that

of R6G. The results indicated the selective adsorption on CNCs, which means R6G was used as the fluorescent dye for labelling CNCs. The corresponding fluorescent spectra in Figure 2.5b also proved the selective adsorption of R6Gs onto CNCs, the fluorescent intensity of PEG2000 with R6G was little decreased while the fluorescent intensity of CNC or CNC/PEG2000 with R6G had dropped around 80%.
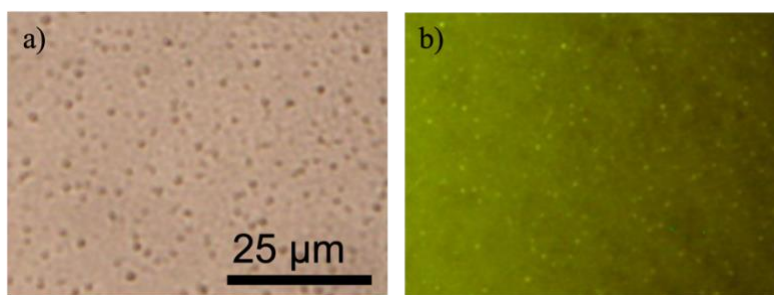
Figure 2.6. Optical images of dried CNCs/PEG2000/R6G. (a) Bright field optical microscope image, (b) fluorescent optical microscope image [24].

The dried samples with R6G were prepared with the same procedure as the samples without R6G and used for component identifications. They were observed with optical microscope and fluorescent optical microscope as illustrated in Figure 2.6. The optical microscope image of these R6G labelled sample in Figure 2.6a was nearly the same as that in non-R6G labelled samples as shown in Figure 2.3, where numerous monodisperse spherical particles around 1 μ m with clear bright shells and dark gray cores were observed. This indicated the R6G introduction did not affect the CNC-PEG2000 core-shell fabrication. In the fluorescent images, numerous small bright-green dots

corresponding to the cores were visible. This indicated that the core of CNC-PEG2000
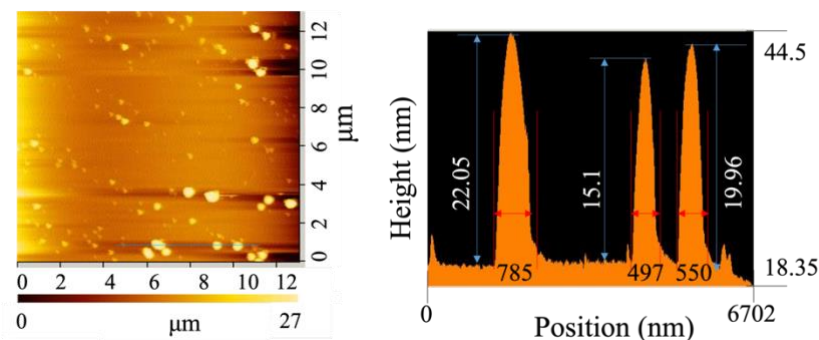
particulates consist of CNCs.

Figure 2.7. AFM topological image of dried CNCs/PEG2000/R6G with cross section [24].

Furthermore, we investigated 3-dimensional morphology of the fabricated

particles, AFM observation were illustrated in Figure 2.7. Particulates with diameters of

ca. 500 nm and height of ca. 20 nm were observed. We calculated particulate diameters

from the AFM images that were smaller than from optical microscope image; this can be

attributed to the higher resolution in detection by AFM. In this case, only the CNC core

parts could be visualized, since the PEG2000 shell could be detected as a lower height.

Furthermore, shells made of PEG2000 could diffuse to the exterior because of the smaller

molecular weight of PEG and because of the absence of the constraints to PEG diffusion

in the shell. This interpretation could explain the smaller diameters for CNC/PEG2000 in

AFM, although further structural investigation, including an investigation in wet state,

should be performed.

2.4. Conclusion

In summary, we have reported a simply approach for preparing CNC-PEG core-shell particles with CNC cores via a SORP method. The particles formation was carried out by simply evaporation of good solvent from solution containing two solvents and two solutes with a different solubility to remaining solvent. Introducing PEG2000 as one component which has better solubility than CNC in EG enables us to fabricate CNC-core PEG-shell particles.

References

1. J. -F. Revol, L. Godbout, X. -M. Dong, D. G. Gray, H. Chanzy, G. Maret. Chiral nematic suspensions of cellulose crystallites; phase separation and magnetic field orientation. *Liq. Cryst.*, 1994, **16**, 127-134.

2. M. Mariano, N. EI Kissi, A. Dufresne. Cellulose nanocrystals and related nanocomposites: Review of some properties and challenges. *J. Polym. Sci., Part B: Polym. Phys.*, 2014, **52**, 791.

3. Y. Xu, A. Atrens, J. R. Stokes. A review of nanocrystalline cellulose suspensions: Rheology, liquid crystal ordering and colloidal phase behaviour. *Adv. Colloid Interface Sci.*, 2020, **275**, 102076.

4. C. Miao, W. Y. Hamad. Critical insights into the reinforcement potential of cellulose nanocrystals in polymer nanocomposites. *Curr. Opin. Solid State Mater. Sci*., 2019, **23**, 100761.

5. S. Belbekhouche, J. Bras, G. Siqueira, C. Chappey, L. Lebrun, B. Khelifi, S. Marais, A. Dufresne. Water sorption behavior and gas barrier properties of cellulose whiskers and mcrofibrils films. Carbohydr. Polym., 2011, **83**, 1740-1748.

6. N. Bumbudsanpharoke, S. Kwon, W. Lee, S. Ko. Optical response of photonic cellulose nanocrystal films for a novel humidity indicator. *Int. J. Biol. Macromol.*, 2019, **140**, 91-97.

7. H. Oguzlu, C. Danumah, Y. Boluk. Colloidal behavior of aqueous cellulose nanocrystal suspensions. *Curr. Opin. Colloid Interface Sci.*, 2017, **29**, 46-56.

8. Y. Nishiyama, P. Langan, H. Chanzy. Crystal structure and hydrogen-bonding system in cellulose Iβ from synchrotron X-ray and neutron fiber diffraction. *J. Am. Chem. Soc.*, 2002, **124**, 9074-9082.

9. F. V. Ferrira, I. F. Pinheiro, R. F. Gouveia, G. P. Thim, L. M. F. Lona. Functionalized cellulose nanocrystals as reinforcement in biodegradable polymer nanocomposites. *Polym. Compos.*, 2018, **39**, E9-E29.

10. A. Anzlovar, M. Huskic, E. Zagar. Modification of nanocrystalline cellulose for application as a reinforcing nanofillers in PMMA composites. *Cellulose*, 2016, **23**, 505-518.

11. J. George, SN Sabapathi. Cellulose nanocrystals: synthesis, functional properties, and applications. *Nanotechnol. Sci. Appl.*, 2015, **8**, 45-54.

12. A. Dufresne. Cellulose nanomaterial reinforced polymer nanocomposites. Curr. Opin. *Colloid Interface Sci.*, 2017, **29**, 1-8.

13. Y. Li, J. J. Y. Suen, E. Prince, E. M. Larin, A. Klinkova, H. T. Aubin, S. Zhu, B. Yang, A. S. Helmy, O. D. Lavrentovich, E. Kumacheva. Colloidal cholesteric liquid crystal in spherical confinement. *Nat Commun*, 2016, **7**, 12520.

14. R. M. Parker, B. F.Petesic, G. Guidetti, G. Kamita, G. Consani, C. Abell, S. Vignolini. Hierarchical self-assembly of cellulose nanocrystals in a confined geometry. *ACS Nano,* 2016, **10**, 8443-8449.

15. P. X. Wang, W. Y. Hamad, M. J. Maclachlan. Polymer and mesoporous silica microspheres with chiral nematic order from cellulose nanocrystals. *Angew. Chem. Int. Ed.*, 2016, **55**, 12460.

16. F. Jativa, C. Schutz, L. Bergsrom, X. Zhang, B. Wicklein. Confined self-assembly of cellulose nanocrystals in a shrinking droplet. *Soft Matter*, 2015, **11**, 5374-5380.

17. H. Yabu, T. Higuchi, M. Shimomura. Unique phase-separation structures of block-copolymer nanoparticles. *Adv. Mater.*, 2005, **17**, 2062-2065.

18. H. Yabu. Creation of functional and structured polymer particles by Self-organized precipitation (SORP). *Bull. Chem. Soc. Jpn.*, 2012, **85**, 265-274.

19. H. Yabu. Self-organized precipitation method: an emerging method for preparation of unique polymer particles. *Polym. J.,* 2013, **45**, 261-268.

20. S. Kawaguchi, K. Ito. Dispersion polymerization. *Adv. Polym. Sci.*, 2005, **175**, 299-328.

21. M. Okubo, J. Izumi, T. Hosotani, T. Yamashita. Production of micro-sized monodispersed core/shell polymethyl methacrylate/polystyrene particles by seeded dispersion. *Colloid Polym. Sci.*, 1997, **275**, 797-801.

22. P. A. Lovell, F. J. Schork. Fundamentals of emulsion polymerization. *Biomacromolecules*, 2020, **21**, 4396-4441.

23. L. J. Borthakur, T. Jana, S. K. Dolui. Preparation of core-shell latex particles by emulsion co-polymerization of styrene and butyl acrylate, and evaluation of their pigment properties in emulsion paints. *J. Coat. Technol. Res.*, 2010, **7**, 765-772.

24. J. Zhang, H. Furushima, T. Nakato, E. Mouri. Preparation of cellulose nanocrystal based core-shell particles with tunable component location. *Chem. Lett.*, 2021, **50**, 240-243.

Chapter 3. Fabrication of CNC-polymer core-shell particles

with CNC shells

Chapter 3. Fabrication of CNC-polymer core-shell particles with CNC shells

3.1. Introduction

In chapter 2, the author had successfully fabricated the cellulose nanocrystal-core particles with the self-organized precipitation (SORP) method [1, 2, 3, 4, 5], with usage low molecular polyethylene glycol (PEG2000) as the polymer component, based on the solubility differences of two solutes in the poor solvent. Principally, SORP can make either CNC-core particle and CNC-shell particle by choosing appropriate counterpart solute and solvents. Fabrication both types of core-shell particles can show the more generalized way to control particle morphology on demand. No previous studies have reported for these types of particle fabrication containing CNC and it would be a worthwhile challenge.

PEG used in the former chapter do not only have non-toxicity characteristics that suits combination with CNCs for development of sustainable materials, but also, the affinity between PEG and solvent can be drastically changed through the molecular weight [6, 7, 8]. In this case, just with molecular weight adjustment, the CNC shell particulates ate expected to be fabricated with the same SORP method.

By fabricating the particulates having a CNC crust, a stable micro-space with cellulose walls similar to those of the plant cells, resulting in a bio-inspired material with high mechanical strength can be realized [9, 10, 11]. Such CNC-shell particles have mainly been prepared with the Pickering emulsion approach and used in food, biomedical and cosmetic applications [12, 13, 14, 15, 16].

In this chapter, we reported the fabrication of CNC-shell particles via the SORP method.

3.2. Experimental

In the experiment, CNCs and polyethylene glycol with average molecular weight of 20000 (PEG20000) were used as two solutes, and water and ethylene glycol (EG) were still used as the two solvents. Figure 3.1 shows the schematic representation of the SORP method applied to the CNC-PEG20000 solute in the water-EG system for CNC-shell particle fabrication. First, CNCs and PEG20000 are dissolved in water (Figure 3.1a), and EG is added to the solution (Figure 3.1b). Water then be evaporated, while EG remains unevaporated (Figure 3.1c). In this process, CNC and PEG20000 tend to deposit because of their decreased solubility in EG. While, opposite to the PEG2000 case, the solubility of CNC in EG is higher than that of PEG20000 in EG, CNC has higher

affinity to EG than that of PEG20000-EG.　With such a fact, the formation of CNC-shell
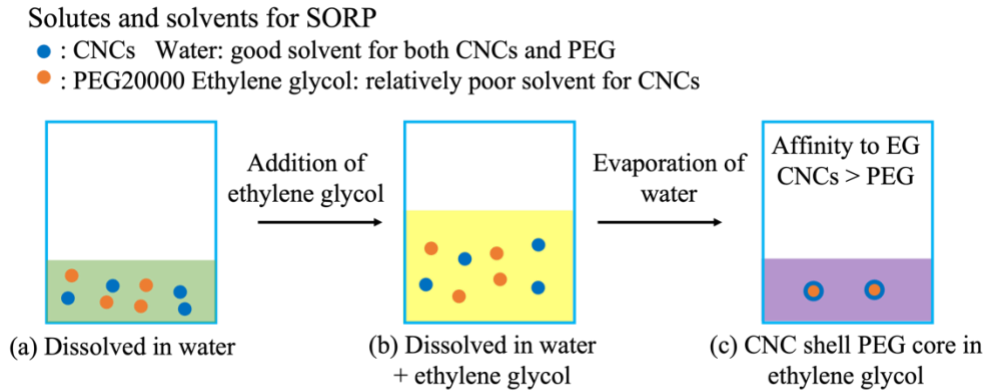
particles can be expected.

Figure 3.1. Schematic process for fabrication of CNC-shell particles via SORP method [17].

For preparation of CNC-shell particles, polyethylene glycol of weight 20000

(PEG20000) was applied as the polymer component, instead of PEG2000 as described in

Chapter 2.

The fabrication method was the SORP method as described in Chapter 2. Briefly,

CNCs and PEG20000 were separately dispersed in Mill-Q water and mixed. Then

ethylene glycol was gradually added into the system for preparing a mixture of CNCs (1

g L^{-1}) and PEG20000 (1 g L^{-1}) in the water/ethylene glycol solvent mixture.

For obtaining the CNC-shell particles, the mixtures were heated at 45°C to

evaporate half the volume in order to remove the water and obtain EG solution. For

further characterization of particles, small amounts of dispersion were dropped on slide

glass and dried in a 40°C vacuum oven for two days to dry completely.

48

The samples at different stage of solvent evaporation were observed with optical microscope. The component identification was also finished with usage of rhodamine 6G as the probe dye. Its selective adsorption was confirmed with UV-vis and fluorescent measurement. For the final particle component and morphology confirmation, the fluorescent optical microscope and atomic force microscope observations were applied.

3.3 Results and discussion
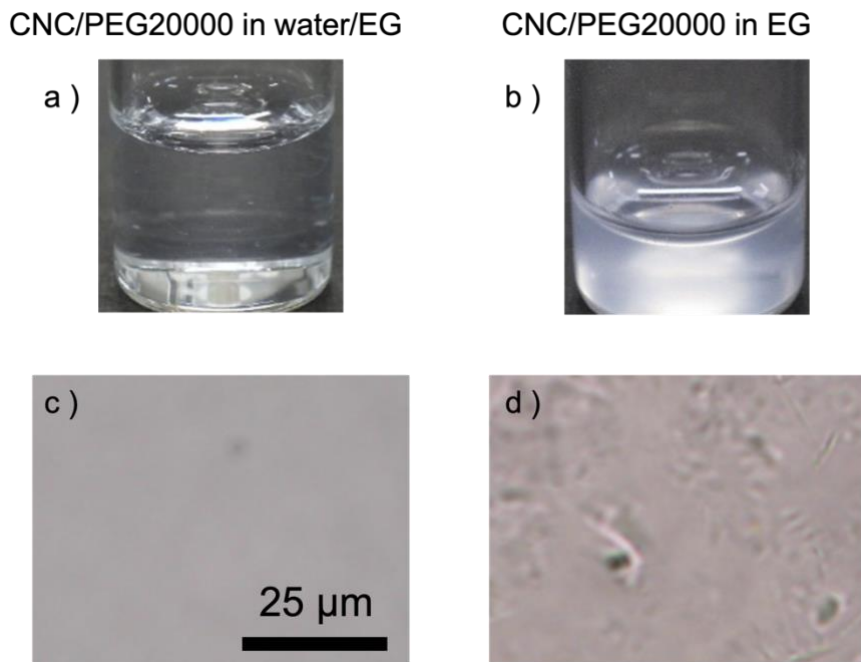
Figure 3.2. Appearance of CNC/PEG20000 in water/EG (a), EG (b) observed with naked eye and CNC/PEG20000 in water/EG (c), EG (d) observed with optical microscope [17]

The appearance of CNC/PEG20000 in the process of SORP were presented in Figure 3.2. The CNC/PEG20000 in water/EG mixture solvent was transparent as shown in Figure 3.2a. Its optical microscope image illustrated in Figure 3.2c also indicated no

particle existence. When the water was evaporated, CNC/PEG20000 left in ethylene glycol turned turbid as shown in Figure 3.2b, which was different from the CNC/PEG2000 with water evaporation. In its corresponding optical microscope image as illustrated in Figure 3.2d, we could not clearly observe the particle formation, only confirm the fluctuation in the contrast of the optical microscopy image.

To confirm the particle formation, a small amount of solution was dried in vacuum oven and observed with optical microscope as illustrated in Figure 3.3. The image indicated the formation of numerous particles with irregular shapes. The particles with size ranging from 2 μ m to several μ m were obtained. In the case of the larger particles, core-shell-like contrast was observed in the images, with dark, irregular shells surrounding brighter cores.
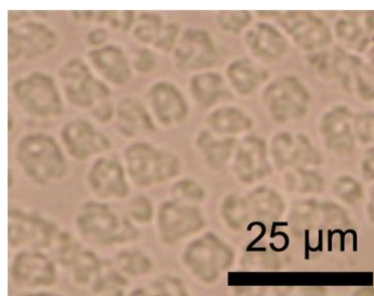
Figure 3.3. Optical microscope image of dried CNC/PEG20000 [17].

Independently, we checked the dispersibility of two components, PEG20000 and CNC, in EG as shown in Figure 3.4. CNC was partly dispersed in EG (a) and PEG20000 was insoluble in EG (b). Based on the higher solubility of CNC in Figure3.4, affinity of

CNC to EG would be higher than that of PEG20000.   Thus, CNC shell formation is more

reasonable to occur if the particles are obtained with this system by SORP.
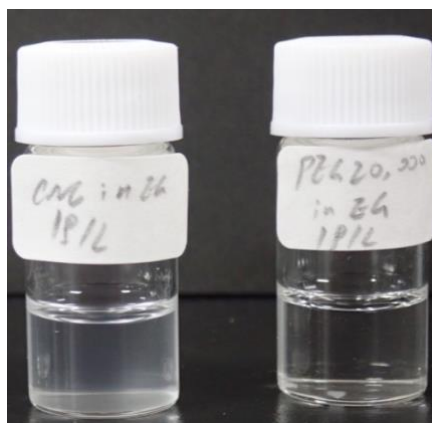

Figure 3.4. Solubility appearance of 1 g L $^{-1}$ CNC (a) and PEG20000 (b) in ethylene glycol

To identify the core-shell components, R6G was introduced into the system. The

selective adsorption of R6G was confirmed with UV-vis and fluorescent spectra as

illustrated in Figure 3.5. The concentration of CNCs or PEG20000 in water was 1 g L $^{-1}$

and R6G concentration was 1.23 x 10^{-5} mol L $^{-1}$.
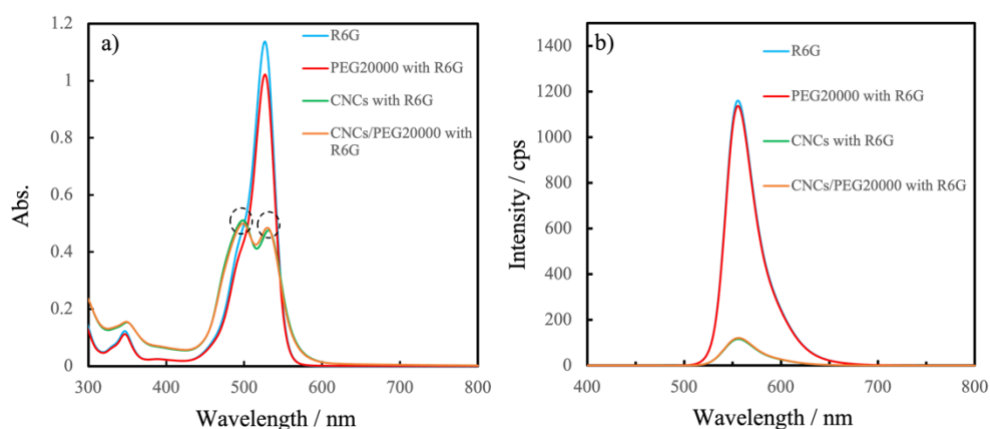
Figure 3.5. UV-vis spectra (a) and fluorescent spectra (b) of various combinations of samples in water containing 1g L $^{-1}$ solutes and 1.23 x 10 $^{-5}$ mol L $^{-1}$, the excitation wavelength in fluorescent measurement is 347 nm [17].

Similar to the CNC/PEG2000 case as described in Chapter 2, PEG20000 mixing

with R6G did not change the UV-vis wavelength of adsorption peak, while wavelength

of adsorption peaks of CNCs and CNCs/PEG20000 mixing with R6G had split into two

different wavelengths as illustrated in Figure 3.5a. This indicated the selective adsorption

of R6G onto CNCs. Meanwhile, the fluorescent spectra of different solutes with R6G also

proved the selective adsorption of CNCs onto CNCs. As illustrated in Figure 3.5b, the

fluorescent intensity of PEG20000 with R6G were nearly the same as that of pristine R6G,

while the fluorescent intensity of CNCs and CNCs/PEG20000 with R6G were greatly

decreased compared to that of pristine R6G.
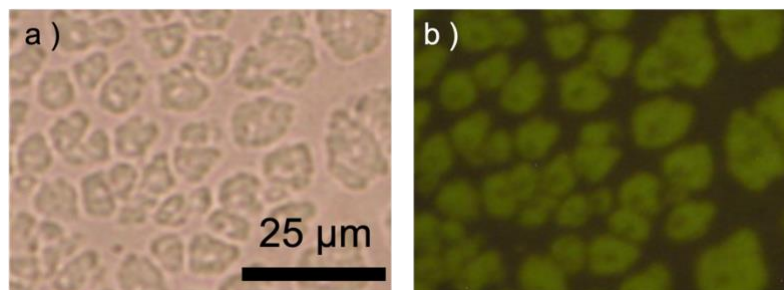
Figure 3.6. Optical images of dried CNCs/PEG20000/R6G. (a) Bright field optical microscope image, (b) fluorescent optical microscope image [17].

The dried samples with R6G were prepared with the same procedure as the

sample without R6G and used for component identifications. They were observed with

optical microscope and fluorescent optical microscope as illustrated in Figure 3.6. The

optical microscope images of CNCs/PEG20000 containing R6G in Figure 3.6a showed

similar images without R6G, which indicated that the addition of R6G did not change the

morphology of the core-shell particulates. In its corresponding fluorescent image as illustrated in Figure 3.6b, core-shell-like particles were observed, which showed bright-green shells (rims) and darker particulate centers. The results of fluorescent optical microscope image suggested that CNCs located in the shell.
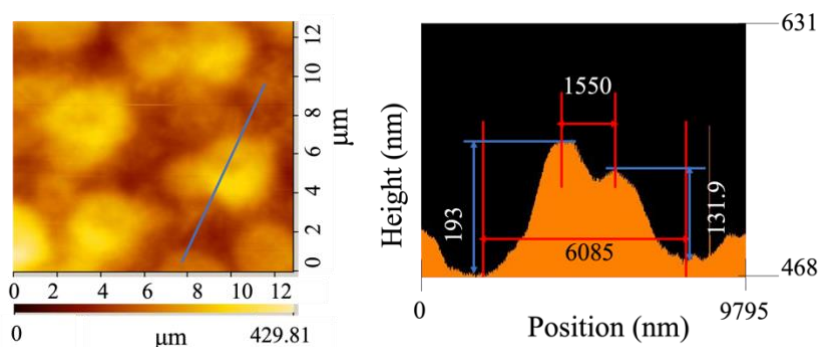
Figure 3.7. AFM topological image of dried CNCs/PEG20000/R6G with cross section [17].

Furthermore, we investigated 3-dimensional morphology of the fabricated particulate, AFM image of dried CNC/PEG20000/R6G was illustrated in Figure 3.7. The particulates observed by AFM were donut-shaped, with a small cavity in the center. This confirmed the core-shell-like structure visualized by optical microscope in Figure 3.6a. The particle diameter was found to be about 6 μm, which was comparable to the diameter obtained from the optical microscope image. The cross-sectional view indicated that the height was 100-200 nm. The cavity had a depth of several tens of nanometers, but it had a certain height relative to the background, which suggested that this was not a simple hole but it was filled with a PEG20000 component.

In Chapter 2 and Chapter 3, we reported a simple approach for preparing cellulose nanocrystal (CNC)-based core-shell particles via modified SORP method in which particle formation was carried out by simply evaporation of solvent containing solutes with different solubility. In the study, we showed that the molecular weight of polyethylene glycol (2000 vs 20000) changes the resultant particulate's morphology, CNC location, shape and size.

We hypothesized that the differences in composition location were due to slight differences in affinity between CNC-EG and PEG-EG. All the components are soluble in water and water/EG mixed solvent, while the solubility of PEG in EG is slightly different, depending on the molecular weight. PEG20000 is insoluble, PEG2000 is soluble in EG. In the CNC/PEG2000 system, PEG2000 has a higher affinity to EG than CNCs, which results in a core-shell structure with a PEG2000 shell. By contrast, CNC has a higher affinity to EG compared with PEG20000. This results in the formation of a core-shell structure, with CNC forming the shell. The difference in affinity to EG has a significant effect on the morphology. The affinity between the polymer and solvent can change drastically with the molecular weight as reported here. These polymer characteristics can be applied to control the morphology without changing the component itself.

3.4. Summary

In summary, we have demonstrated a simply approach for preparing CNC-core and CNC-shell particles via modified self-organized precipitation (SORP) method just by changing polymer molecular weight.   On the basis of these findings in Chapter 2 and 3, we expect that core-shell particles with similar composition can be designed to include CNCs in different locations by other polymers and their morphologies can be manipulated by the control over the polymer-solvent interactions, which can enrich the applications of this particulate composite system.

References

1. H. Yabu. Self-organized precipitation: an emerging method for preparation of unique polymer particles. *Polym. J.*, 2013, **45**, 261-268.

2. H. Yabu, K. Koike, K. Motoyoshi, T. higuchi, M. Shimomura. A novel route for fabricating metal-polymer composite nanoparticles with phase-separated structures. *Macromol. Rapid Commun.*, 2010, **31**, 1267-1271.

3. H. Yabu, T. Higuchi, M. Shimomura. Unique phase-separation structures of block-copolymer nanoparticles. *Adv. Mater.*, 2005, **17**, 2062-2065.

4. H. Yabu, T. Higuchi, K. Ijiro, M. Shimomura. Spontaneous formation of polymer nanoparticles by good-solvent evaporation as a nonequilibrium process. *Chaos,* 2005, **15**, 047505.

5. H. Yabu, S. Sato, T. Higuchi, H. Jinnai, M. Shimomura. Creating suprapolymer assemblies: nanowires, nanorings, and nanospheres prepared from symmetric block-copolymers confined in spherical particles. *J. Mater. Chem.*, 2012, **22**, 7672-7675.

6. Wiley-VCH, Polyethylene glycol (MAK Value Documentation, 1998) in The MAK-collection for occupational health and safety. *Wiley-VCH*, 2012, **248**, 70.

7. C. Ozdemir, A. Guner. Solubility profiles of poly(ethylene glycol)/ solvent systems, I: qualitative comparison of solubility parameter approaches. *Eur. Polym. J.*, 2007, **43**, 3068-3093.

8. K. Adamska, A. Voelkel. Hansen solubility parameters for polyethylene glycols by inverse gas chromatography. *J. Chromatogr. A*, 2006, **1132**, 260-267.

9. H. Dai, J. Wu, H. Zhang, Y. Chen, L. Ma, H. Huang, Y. Huang, Y. Zhang. Recent advances on cellulose nanocrystals for Pickering emulsions: Development and challenge. *Trends Food Sci. Technol*., 2020, **102**, 16-29.

10. T. Nypelo, C. R. Abreu, Y. V. Kolen'ko, J. Rivas, O. J. Rojas. Microbeads and hollow microcapsules obtained by self-assembly of Pickering magneto-responsive cellulose nanocrystals. *ACS Appl. Mater. Interfaces*, 2014, **6**, 16851-16858.

11. C. Ye, S. T. Malak, K. Hu, W. Wu, V. Tsukruk. Cellulose nanocrystal microcapsules as tunable cages for nano- and microparticles. *ACS Nano*, 2015, **9**, 10887-10895.

12. H. Yan, X. Chen, M. Feng, Z. Shi, W. Zhang, Y. Wang, C. Ke, Q. Lin. Entrapment of bacterial cellulose nanocrystals stabilized Pickering emulsions droplets in alginate beads for hydrophobic drug delivery. *Colloids Surf. B*, 2019, **177**, 112-120.

13. S. Fujisawa, E. Togawa, K. Kuroda. Nanocellulose-stabilized Pickering emulsions and their applications. Sci. Technol. *Adv. Mater.*, 2017, **18**, 959-971.

14. M. Marquis, V. Alix, I. Capron, S. Cuenot, A. Zykwinska. Microfluidic encapsulation of Pickering oil microdroplets into alginate microgels for lipophilic compound delivery. *ACS Biomater. Sci. Eng.*, 2016, **2**, 535-543.

15. Z. Zhang, K. C. Tam, X. Wang, G. Sebe. Inverse Pickering emulsion stabilized by cinnamate modified cellulose nanocrystals as templates to prepare silica colloidosomes. *ACS Sustainable Chem. Eng.*, 2018, **6**, 2583-2590.

16. H. Dou, M. Jiang. Fabrication, characterization and drug loading of pH-dependent multi-morphological nanoparticles based on cellulose. *Polym. Int.*, 2007, **56**, 1206-1212.

17. J. Zhang, H. Furushima, T. Nakato, E. Mouri. Preparation of cellulose nanocrystal based core-shell particles with tunable component location. *Chem. Lett.*, 2021, **50**, 240-243.

Chapter 4. Linear assembly of colloidal inorganic nanosheets:

evaluation of the linearity

Chapter 4. Linear assembly of colloidal inorganic nanosheets: evaluation of the linearity

4.1. Introduction

As described in Chapter 1, hierarchical structures of inorganic nanosheets have relatively been unexplored compared with those of CNC rods. Compared with the organization of 1D particles, that of 2D particles is characterized by diversity of the organized structures [1, 2, 3]. While the 1D particles are morphologically uniaxial, 2D particles are biaxial [4, 5]. This means larger freedom of the orientation of 2D particles, and leads to complexity and difficulty of assembling 2D particles [6].

As an example of such complexity, hierarchical organization of aqueous colloidal niobate nanosheets under an AC electric field has been developed [7, 8]. Because of the 2D nature of nanosheets, two orthogonal external forces are necessary for aligning them in a unidirectional manner, being in contrast with 1D particles that can be unidirectionally aligned by a single external force [9, 10]. Nakato et al. have constructed macroscopic hierarchical structures reflecting 2D nature of inorganic nanosheets using colloidal hexaniobate ($[Nb_6O_{17}]^{4-}$) nanosheets [9, 11, 12, 13] with the strategy of combining nanosheet domain growth based on internal nanosheet–nanosheet interactions

and nanosheet alignment under external electric fields. They employed the two-stage process, where the nanosheet domains, which are called tactoids hereafter, grow at the first stage, and application of an AC electric field at the second stage orient the tactoids to yield the final structure [7].

The final structure obtained by the two-stage nanosheet organization depends on the relative direction of the applied electric field and gravity [7, 8]; a net-like texture is obtained by the application of the two external forces from the same direction while a stripe texture forms by the orthogonal application, as schematically depicted in Figure 4.1. Particularly, the stripe texture is a linearly assembled texture characterized by the length of more than 1 mm. The structure is characterized by the unidirectional alignment of the nanosheets with the lateral size of 1–2 μm.   Such a structure is important because of its applicability for various uses that require a specific orientation of nanosheets [14]. Nanosheet ordering with higher linearity provides more highly anisotropic optical, electronic, and physicochemical functions [7, 15, 16], in sharp contrasts with conventional materials with isotropic structures.

Because the stripes of more than 1 mm length are constructed by the linear alignment of nanosheets with lateral length of micrometers, the linearity of stripes is determined by the alignment of individual nanosheets, and thus greatly affected by

conditions of the colloidal nanosheets.　However, evaluation methods of the stripe

linearity have yet been developed.　Therefore, the author proposes herein a method for

quantitatively evaluating the linearity of the stripe structures constructed by the colloidal
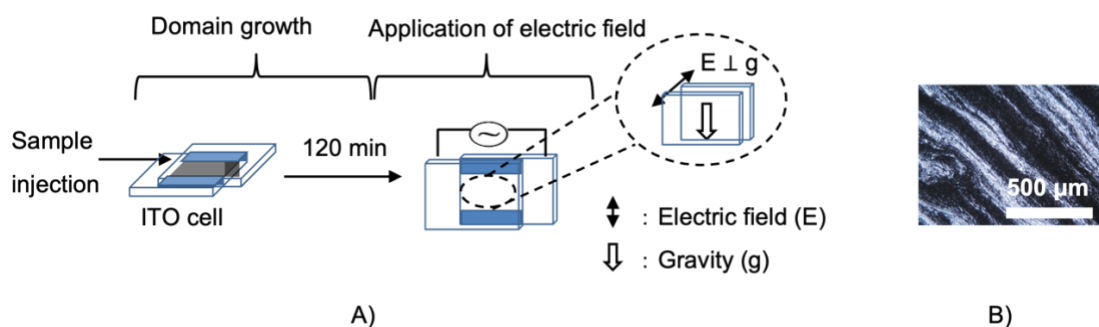
niobate nanosheets.

Figure 4.1. (a) Schematic representation of the experimental procedure for constructing colloidal stripes of the niobate nanosheets, and (B) an example of the stripe observed by polarized optical microscopy.　The electric field is applied from the direction perpendicular to gravity.　The arrows indicate the direction of electric field (E) and gravity (g), respectively [18].

4.2. Experimental

4.2.1. Sample preparation and instrumentation

　　　Milli-Q water was used in all of the experiments.　A colloidal sample of the

niobate nanosheets was prepared by the method reported previously. Briefly,

tetrapotassium hexaniobate $K_4Nb_6O_{17}$ was treated with a 0.2 mol L^{-1} aqueous

propylammonium chloride solution at 120 °C for a week in a Teflon-lined stainless steel

autoclave.　Then, solid product was centrifuged, washed and dialyzed with water to yield

the initial stock colloid sample.　With these treatments, the layered niobate crystals were exfoliated to form of niobate nanosheet colloids, where the negatively charged niobate nanosheets were accompanied by propylammonium cations that were introduced as an exfoliating reagent for the niobate crystal via replacing the interlayer K^+ ions [7, 17].

　　The texture formation was finished by the procedure described below.　A small portion of the colloids was injected into a thin-layer cell, built up with two ITO-coated glass plates sandwiching a 100 μm film spacer.　The sample injected into the cell was let stand for 120 min to allow the growth of tactoids by standing the cell with the "flat" cell setting (i.e., at the horizontal position, Figure 4.1 left) under ambient conditions. Then, an AC electric field (500 V cm $^{-1}$, 50 kHz) was applied to the colloid sample in the thin layer cell [7, 9].　The electric field was at first applied to the cell with the flat setting for a second.　The cell was then turned to the upright position, which was maintained until the end of the observation.　In this cell setting, the electric field and gravity were applied from the orthogonal directions, which assembled nanosheets into stripes along gravity.　The texture formation was observed with Olympus BX-51 polarized optical microscope (POM).

4.2.2. Principle of the evaluation of stripes

The stripes consist of the unidirectionally aligned colloidal niobate nanosheets, are detected by polarized optical microscopy (POM).   The POM technique observes birefringence of the nanosheet domains electrically aligned parallel to the electric field. Tight bundling of nanosheets in the aligned nanosheet domains give intense birefringence. The stripe texture is provided by the flow-induced orientation of the electrically aligned nanosheets.   Long and straight stripes are obtained by long-range unidirectional orientation of the nanosheets.   Thus, regularity and linearity of the nanosheet alignment into the stripes are reflected by the intensity and uniformity of the birefringence of the stripes in the POM images.   The author expresses regular and linear stripes with high birefringence and uniformity as "good stripes".

For the quantitative evaluation of the stripes, the author analyzed brightness of the pixels of POM images using Image J software, and estimated contrast of white (bright) to black (dark) areas.   The author evaluated the brightness (gray value) from parallel and transverse directions with respect to the stripes, for each POM image.   Contrast of the bright and dark parts in each direction was estimated based on the largest and lowest gray values of pixels in each direction.   Then, "ratio of contrast" (RC) was estimated as the quotient of the contrast across stripe and that along stripe, as schematically shown in Figure 4.2 on the basis of the following idea.   If ideal stripes are generated, each stripe

is homogeneously white in their longitudinal direction to give the contrast along the stripe being unity while the contrast across the stripe much larger than 1. This situation resultsin the RC value much larger than 1. However, if the texture is an ideal net, the contrasts in the two orthogonal directions should be the same, giving the RC value of 1.
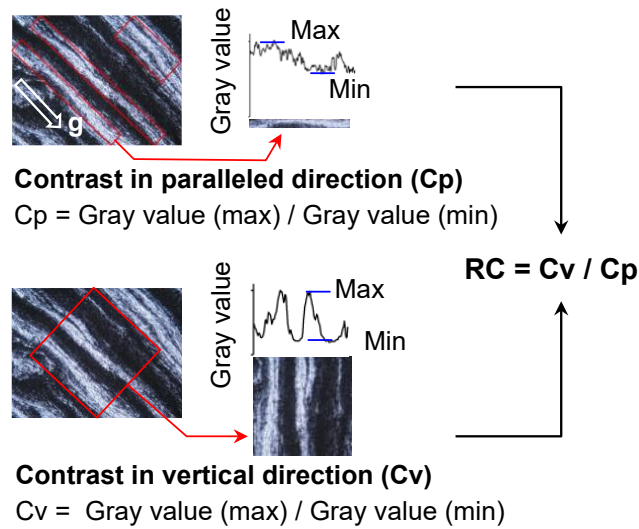

Contrast in paralleled direction (Cp)
Cp = Gray value (max) / Gray value (min)

RC = Cv / Cp

Contrast in vertical direction (Cv)
Cv = Gray value (max) / Gray value (min)

Figure 4.2. Schematic representation of the procedure for evaluating the ratio of contrast (RC) value of the stripes of the linearly aligned nanosheets [18].

4.2.3. Evaluation process

POM images of the real samples, which involve inhomogeneity of the width, linearity, and brightness of stripes, were analyzed by the following procedure. The quality of the stripes is characterized by the uniformity and homogeneity of the stripes along *g* direction observed by POM in which *g* with arrow stands for the direction of gravity. In our POM images, nanosheets are localized in bright (white) part. In principle, we estimate the brightness (gray value) contrasts in the two directions, that is, the contrast in

longitudinal direction (Cp) and the contrast in transverse direction (Cv).   Then we take

the quotient of the contrast across stripe (Cv) and that along stripe (Cp), which we defined

as "ratio of contrast" (RC).   RC represents a degree of an anisotropic character of an

image.   For example, RC is almost 1 if the image is isotropic, and RC is much larger
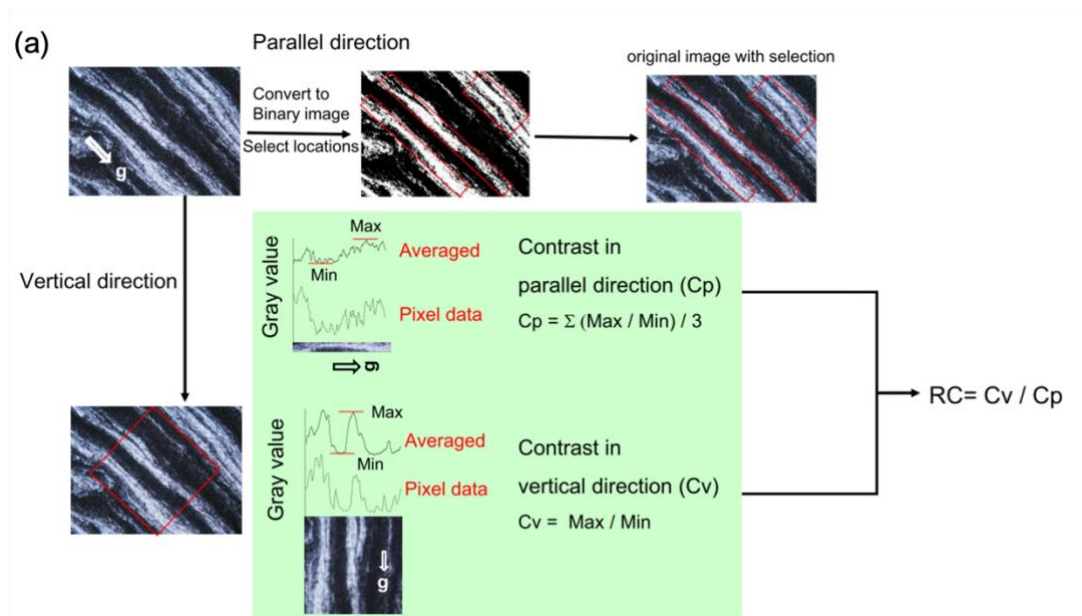
than 1 if the ideal stripes are obtained.
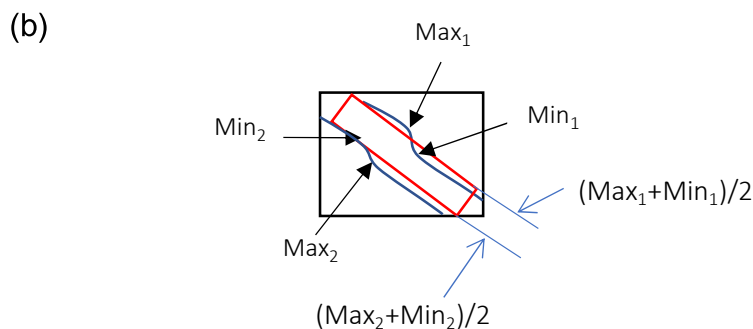
Figure 4.3. Schematic representations of (a) image analysis procedure for obtaining "ratio of contrast (RC)" values and (b) selection of locations for analysis in parallel direction [18].

The image analysis procedure is as described in Figure 4.3. In the first step for estimating Cp, we need to select the places to analyze. In order to define the places for analysis, the raw data image is converted to binary (black and white) image, and we select three rectangles based on the representative stripes as shown in Figure 4.3a. The exact place selection of the stripe is defined as described in the drawing in Figure 4.3b. After the selection of the places, we go back to the original image, and estimate averaged gray values along the longitudinal direction. Taking average of each pixel's gray values along with the transverse direction can be effective for noise-cancelling in the gray values. We take the ratio of the maximum and the minimum gray values for each rectangle and calculate the averaged ratio as Cp.

In the estimation of Cv, we select one square place in the middle of the image, as shown in Figure 4.3a. Then we estimate averaged gray values in transverse direction. Taking average of each pixel's gray values along with the longitudinal direction can be effective for noise-cancelling in the gray values. We take the ratio of the maximum and the minimum gray values and calculate the ratio as Cv. By using the two obtained vales Cp and Cv, we calculated RC (= Cv/Cp). We used RC as the linearity indicator of the high contrast and straightness of the stripes.

4.3. Results and discussion

4.3.1. Evaluation results
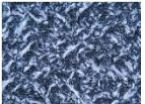
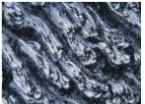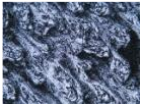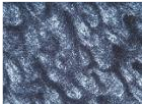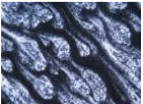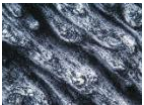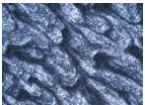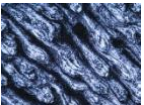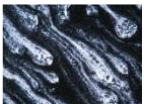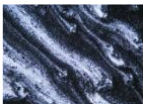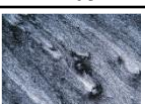| Texture type	Polarized optical microscope (POM) images and RC values					
Net-like	RC: 0.72	0.81	0.93			
Drop-like	0.50	0.53	0.60	0.72	0.77	0.77
	0.78	0.83	0.88	0.90	0.93	0.95
	1.05	1.21	1.27	1.31	1.49	
Poor-stripe	0.81	1.25	1.29	1.34	1.41	
Good-stripe	3.10					

Figure 4.4. Polarized optical microscope images of water-treated samples with their corresponding Ratio of contrast (RC) values, the textures are classified depending on texture types. A and P indicate the directions of analyzer and polarizer, g indicate gravity, respectively. The scale bar is 500 μm [18].

We purified niobate nanosheet colloids by dialysis with water after exfoliation, and treated with the same procedure, that is, tactoid growth by standing the sample under ambient conditions for 120 min and subsequent electric field application of 5 V 50 kHz AC voltage for 60 min from the direction orthogonal to gravity in order to generate the

67

stripe structure at the same nanosheet concentration (5 g L^{-1}).   However, the obtained

texture varied with the species and concentration of the coexisting electrolyte introduced

by dialysis of the nanosheet colloids.   Figure 4.4 list all of the POM images of niobate

nanosheet colloids treated by the methods described in 4.2.2.   They involve many

colloid samples dialyzed by water or the electrolyte solutions.   Obviously, stripes are

formed in many samples, but other textures are also formed frequently.   Also, the

regularity and linearity, which are expressed holistically by a word "quality" hereafter, of

the stripes are different with the sample.
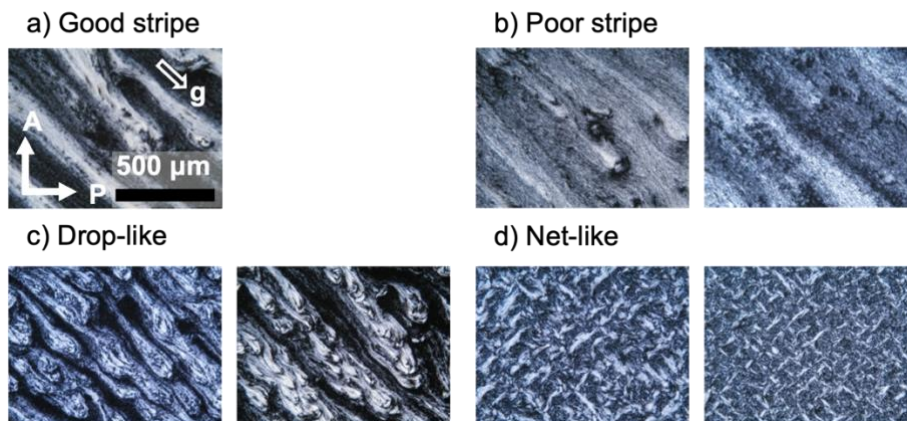
Figure 4.5. Representative polarized optical microscopic images of four texture types assembled from niobate nanosheet colloids purified with water: (a) good stripe, (b) poor stripe, (c) drop-like, (d) net-like (Two samples for each type).   A and P indicate the directions of analyzer and polarizer, g indicate that of gravity, respectively.   Scale bar is 500 µm [18].

Figure 4.5 shows magnified POM images of typical samples extracted from

those in Figure 4.4.   The bright (white) areas indicate birefringence due to the

nanosheets aligned by the AC voltage into perpendicular to the cell surface (parallel to

the AC voltage).　Based on the POM images, we classify the colloid textures into 4 types: good stripe, poor stripe, drop-like, and net-like.　The stripe quality of "good" and "poor" was judged with eyes on the basis of obvious uniformity and homogeneity of the thickness and whiteness in longitudinal direction of each strip as well as the length of stripes. In these electrically driven textures, nanosheets are localized in the birefringent areas, as has been indicated by the fluorescent optical microscopy in previous study [1].

The stripe formation is related to the slow flow of nanosheets under the electric field in the thin-layer cell placed vertical (upright) to the lab bench.　The nanosheets are assembled to tactoids (nanosheet domains), and then the AC voltage is applied.　Good stripes are obtained if the nanosheets forming the tactoids turn their alignment to the direction parallel to the gravity, and the aligned tactoids are stretched and connected along the flow direction. Nanosheets must flow enough in the colloid for realizing this situation. In contrast, if the nanosheets do not flow smoothly along gravity, tactoid deformation and connection are restricted so that a drop-like texture is generated.　A net-like texture indicates the nanosheet alignment with little flow.

4.3.2. Validity of the analysis
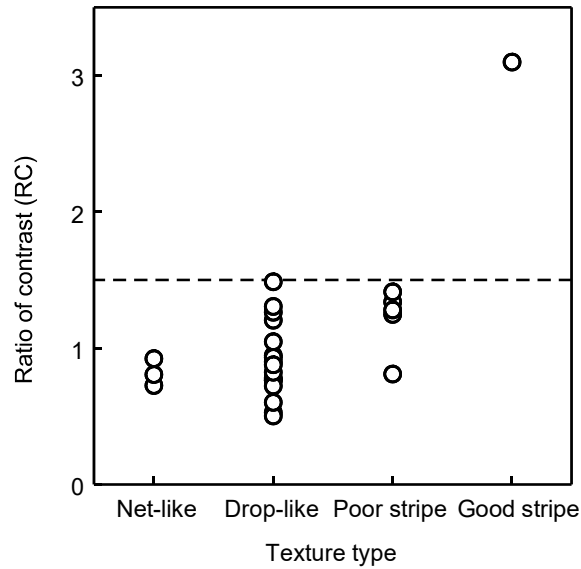
Figure 4.6. Ratio of contrast (RC) values for each texture type (net-like, drop-like, poor stripe, and good stripe) obtained in niobate nanosheet colloids purified with water [18].

Figure 4.6 plots the RC values of the textures generated in the samples listed in Figures 4.4 against the four texture types. These results give a threshold RC value of 1.5 for distinguishing good stripe from the other texture types. The samples of RC > 1.5 are all classified into "good stripe" samples, whereas the samples of RC ≤ 1.5 involve all types of the textures. Hence, we define hereafter the "good stripe" textures by their RC values being larger than 1.5. In fact, Average RC value of all of the samples of this class is 2.0. All of the samples with RC ≥ 1.5 exhibit stripes longer than > 1 mm, indicating long-range unidirectional ordering of nanosheets under the orthogonal application of electric field and gravity. In contrast, the "poor stripe" samples give the average RC value of 1.2, reflecting the lack of long range nanosheet ordering. For the drop-like and

net-like textures, their average RC values are estimated as 0.84 and 0.82, respectively.

These values close to 1 indicate that the nanosheets are little anisotropically ordered along

gravity, in agreement with the observed textures.   Thus, we confirmed the present

evaluation method of RC are valid for evaluating the quality of the stripes formed in a

niobate nanosheet colloid under an AC voltage.

4.4. Summary

Because the higher-ordered stripe texture is important because of its applicability

for various uses that require a specific orientation of nanosheets, suitable method for

evaluating the quality of the stripes is necessary.   The author established a quantitative

evaluation method of analyzing the generated textures by image analysis of polarized

optical microscope images of the samples.   The regularity and linearity of the aligned

domains, which are elongated and connected to form the stripes, are indicated by the Ratio

of Contrast (RC) value.   The RC value matched well with the eye classification of the

textures, which confirmed the availability of present evaluation method for linearity

evaluation.

References

1. Y. Chen, Z. Fan, Z. Zhang, W. Niu, C. Li, N. Yang, B. Chen, H. Zhang. Two-dimensional metal nanomaterials: synthesis, properties, and applications. *Chem. Rev.*, 2018, **118**, 6409-6455.

2. M. Osada, T. Sasaki. Nanosheet architectonics: a hierarchically structured assembly for tailored fusion materials. *Polym. J.*, 2015, **47**, 89-98.

3. M. Osada, T. Sasaki. Two-dimensional dielectric nanosheets: novel nanoelectronics from nanocrystal building blocks. *Adv. Mater.*, 2012, **24**, 210-228.

4. D. Lisjak, A. Mertelj. Anisotropic magnetic nanoparticles: a review of their properties, syntheses and potential applications. *Prog. Mater. Sci.*, 2018, **95**, 286-328.

5. K. J. Lee, J. Yoon, J. Lahann. Recent advances with anisotropic particles. *Curr. Opin. Colloid Interface Sci.*, 2011, **16**, 195-202.

6. T. Nakato, J. Kawamata, S. Takagi. Inorganic nanosheets and nanosheet-based materials. *Springer*, Tokyo, 2017.

7. T. Nakato, Y. Nono, E. Mouri, M. Nakata. Panoscopic organization of anisotropic colloidal structures from photofunctional inorganic nanosheet liquid crystals. *Phys. Chem. Chem. Phys.*, 2014, **16**, 955-962.

8. T. Nakato, Y. Nono, E. Mouri. Textural diversity of hierarchical macroscopic structures of colloidal liquid crystalline nanosheets organized under electric fields. Colloids and Surfaces A: Physicochem. Eng. Aspects, 2017, 522, 373-381.

9. T. Nakato, K. Nakamura, Y. Shimada, Y. Shido, T. Houryu, Y. Iimura, H. Miyata. Electrooptic response of colloidal liquid crystals of inorganic oxide nanosheets prepared by exfoliation of a layered niobate. *J. Phys. Chem. C*, 2011, **115**, 8934-8939.

10. D. Bordel, J. L. Putaux, L. Heux. Orientation of native cellulose in an electric field.

Langmuir, 2006, **22**, 4899-4901.

11. N. Miyamoto, T. Nakato. Liquid crystalline nanosheet colloids with controlled particle size obtained by exfoliating single crystals of layered niobate $K_4Nb_6O_{17}$. *J. Phys. Chem.* B, 2004, **108**, 6152-6159.

12. N. Miyamoto, T. Nakato. Liquid crystalline nature of $K_4Nb_6O_{17}$ nanosheet sols and their macroscopic alignment. *Adv. Mater.,* 2002, **14**, 1267-1270.

13. T. Nakto, N. Miyamoto, A. Harada. Stable liquid crystalline phases of colloidally dispersed exfoliated layered niobates. *Chem. Commun.*, 2004, 78-79.

14. K. Jiang, J. Wang, Q. Li, L. Liu, C. Liu, S. Fan. Superaligned carbon nanotube arrays, films, and yarns: a road to applications. *Adv. Mater.*, 2011, **23**, 1154-1161.

15. T. Huang, Y. Li, M. Chen, L. Wu. Bi-directional high thermal conductive epoxy composites with radially aligned boron nitride nanosheets lamellae. *Compos. Sci. Technol.*, 2020, **198**, 108322.

16. J. Li, S. Wang, L. Lai, P. Liu, H. Wu, J. Xu, S. J. Severtson, W. J. Wang. Synergistic enhancement of gas barrier and aging resistance for biodegradable films with aligned graphene nanosheets. *Carbon*, 2021, **172**, 31-40.

17. N. Miyamoto, T. Nakato. Liquid crystalline inorganic nanosheet colloids derived from layered materials. *Isr. J. Chem.*, 2012, **52**, 881-894.

18. J. Zhang, K. Morisaka, T. Kumamoto, E. Mouri, T. Nakato. Electrolyte-dependence of the macroscopic textures generated in the colloidal liquid crystals of niobate nanosheets. *Colloids Surf. A: Physicochem. Eng. Asp.*, 2018, **556**, 106-112.

Chapter 5. Electrically induced linear assembly of colloidal inorganic nanosheets: experimental conditions necessary for constructing the linear structure

Chapter 5. Electrically induced linear assembly of colloidal inorganic nanosheets: experimental conditions necessary for constructing the linear structure

5.1. Introduction

In Chapter 4, the author has offered a method for quantitatively evaluating the 1D colloidal structure obtained by 2D nanosheets: stripe textures resulted from unidirectional assembly of the colloidal niobate nanosheets. The stripe texture is important because it expands two-dimensionality of the nanosheets with the lateral size of 1–2 μm up to the length of more than 1 mm with retention of their colloidal fluidity and without chemical binding between the nanosheets [1, 2]. This texture is a temporal structure generated by flow induced alignment of the nanosheets with gravity [1,2]. Domains of the colloidal nanosheets grown by standing the colloids under ambient conditions prior to the application of the AC voltage are stretched and connected to form the stripes. The results demonstrate that nanosheet colloids generate various hierarchically organized macroscopic structures on the basis of the 2D particle shape and conditions of the applied external field [1, 2, 3, 4].

However, the author has discovered diversity of the stripe textures even though the same procedure is employed. This will be ascribed to unavoidable fluctuation of the

nanosheet size and movement in the colloids.   Because the nanosheet colloids are aqueous colloids of electrically charged oxide nanosheets, ionic conditions of the colloids should greatly affect the interparticle interactions [5, 6, 7, 8, 9, 10].   This suggests that the colloidal texture of the assembled nanosheets is governed by electrolytes coexisting in the colloids.   Therefore, in this Chapter, the author reports the influence of coexisting electrolyte on the texture formed by the assembly of colloidal niobate nanosheets in the same colloid and by the same procedure.   The regularity and linearity of the stripes are evaluated by the method described in Chapter 4, and correlated with electrolyte conditions. Our results show that more regular and linear stripes are attained under limited ranges provided by the electric conductivity and pH of the colloid.

5.2. Experimental

The niobate nanosheet colloid was prepared and then subjected to the alignment under as AC electric field according to the procedure described in Chapter 4.   The electrolyte-treated samples were prepared by dialyzing above colloidal liquid crystals (LC) with several electrolyte solutions: KCl, K_2CO_3, propylamine, and propylammonium chloride at $10^{-4} — 10^{-2}$ mol L^{-1}.   A small portion of the initial stock sample was dialyzed with an electrolyte solution for 24 h and then diluted to 5 g L^{-1} (indicated by the mass of $Nb_6O_{17}^{4-}$) with corresponding electrolyte solutions.   These treatments allowed

fluctuation of the quality of the stripes formed after the domain growth and electric field application of the colloid.

Values of pH and electric conductivity of the sample were obtained by a Horiba LAQUA act D-71 and LAQUA act D-74 instruments, respectively. Electric conductivity was measured after diluting the sample by water to be 0.1 g L^{-1} nanosheet concentration. The obtained textures were observed by a polarized optical microscope (POM), and characterized by the image analysis written in Chapter 4. The quality of the stripes is indicated by the RC value obtained by the image analysis of the POM images.

5.3. Results and discussion

5.3.1. Electrically induced textures of nanosheet colloids dialyzed with electrolyte solutions

We examined the electric alignment of nanosheet colloids dialyzed with aqueous solutions of electrolytes. KCl, K$_2$CO$_3$, C$_3$H$_7$NH$_3$Cl, and C$_3$H$_7$NH$_2$ were examined because the niobate nanosheets carry both potassium and C$_3$H$_7$NH$_3^+$ ions as countercations of the negatively charge niobate ([Nb$_6$O$_{17}$]$^{4-}$) sheets. All of the textures under the electric field obtained for the samples with electrolyte solutions are indicated

in Figure 5.1. In Figure 5.1, the RC values estimated for individual sample are also
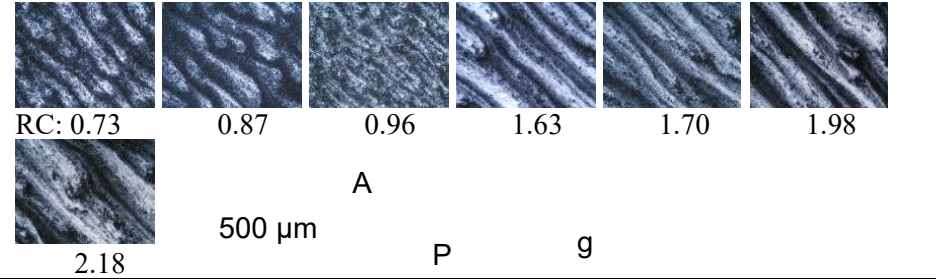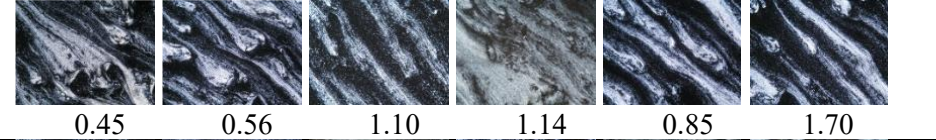
indicated.
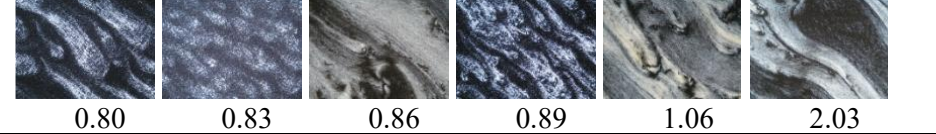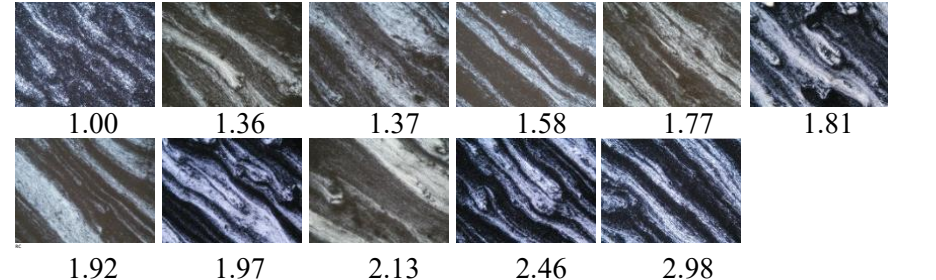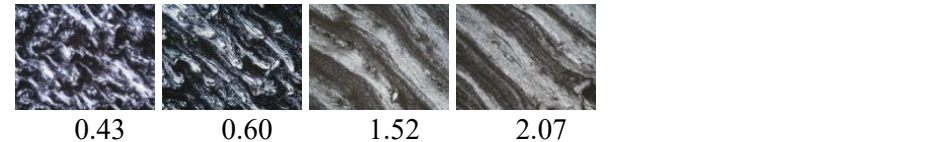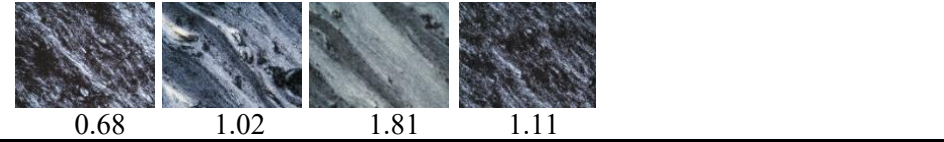
Electrolyte solutions	Polarized optical microscope (POM) images and RC values					
PrNH$_3$Cl (10^{-3} mol L^{-1})	RC: 0.73	0.87	0.96	1.63	1.70	1.98
	2.18	500 µm A P		g		
K$_2$CO$_3$ (10^{-3} mol L^{-1})	0.45	0.56	1.10	1.14	0.85	1.70
PrNH$_2$ (10^{-3} mol L^{-1})	0.80	0.83	0.86	0.89	1.06	2.03
KCl (10^{-3} mol L^{-1})	1.00	1.36	1.37	1.58	1.77	1.81
	1.92	1.97	2.13	2.46	2.98	
KCl (5×10^{-4} mol L^{-1})	0.43	0.60	1.52	2.07		
KCl (2×10^{-3} mol L^{-1})	0.68	1.02	1.81	1.11		

Figure 5.1 Polarized optical microscope images of various electrolyte treated samples with their corresponding Ratio of contrast (RC) values, the textures are classified based on the electrolyte treatments. A and P indicate the directions of analyzer and polarizer, g indicate gravity, respectively. The scale bar is 500 µm [17].
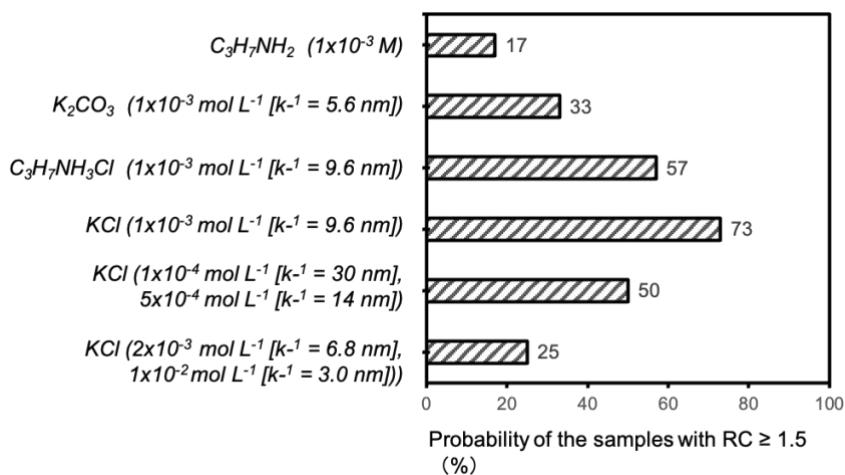
Figure 5.2 Probability of getting good stripe texture for different treatments. The probability is calculated based on the ratio of good stripe sample numbers. Debye length (κ^{-1}) calculated based on the concentrations of electrolytes are presented together in the brackets [17].

Figure 5.2 summarizes percentage of the samples indicating RC > 1.5, i.e. exhibiting "good stripe" textures, after dialysis with different electrolyte species and concentrations. Comparison of the electrolytes at the same concentration of 1×10^{-3} mol L^{-1} indicates that KCl gives RC > 1.5 with the highest probability of 73%. While $C_3H_7NH_3Cl$ gives the probability a little larger than 50%, K_2CO_3 and $C_3H_7NH_2$ give the value much less than 50%. When the concentration of KCl is altered, the highest probability is obtained at 1×10^{-3} mol L^{-1}; concentrations higher and lower than 1×10^{-3} mol L^{-1} give probabilities less than 50% (50% for 5×10^{-4} mol L^{-1}, 25% for 2×10^{-3} mol L^{-1}). These results demonstrate that dialysis with 1×10^{-3} mol L^{-1} KCl is the most appropriate for the formation of stripe texture indicating unidirectional alignment of

79

nanosheets.　In fact, the most clear, straight, and homogeneous stripes with RC > 2,

shown later, are obtained with this condition.

These results demonstrate that the samples after dialysis with electrolytes show

a general tendency of forming stripes with higher probabilities, compared with the

samples only purified with water, i.e., not treated with electrolytes, described in Chapter

4; the water purified samples tend to generate drop-like textures but not stripes, in

particular those of high RC values as shown in Figure 4.6, 5.2.　The less probable stripe

formation in the water-purified samples would be caused by the low concentration of

residual electrolyte which is mainly eliminated by the purification procedure.　Because

clear dependence of the texture on the ion species is not confirmed although the ionic

radii of potassium (0.152 nm) and $C_3H_7NH_3^+$ ions (around 0.347 nm reported for

$(CH_3)_3NH^+$) are different [11], ionic ratios of the electrolyte is not a governing factor.

The electrolyte effect would be related to the contribution of electrical double layers at

the nanosheet surfaces to the texture generation [12, 13, 14].　Thus, we also present the

values of Debye length determined by the electrolyte solutions in Figure 5.2.　The stripe

textures more likely appears when the electrolyte concentration corresponds to the Debye

length of around 10 nm. As to the effects of electrolytes on electric alignment of aqueous

nanosheet colloids, graphene oxide colloids exhibit a decrease in response sensitivity

upon addition of NaCl addition [15] while colloids of beidelite clay nanosheets are insensitive to the presence of NaCl in the concentration range of 10^{-4} to 10^{-5} mol L^{-1} [16]. Our system is more like the latter, which is reasonable considering the intrinsic surface charge of the niobate nanosheets.

5.3.2. Conditions of nanosheet colloids for high linearity

Although the stripe textures are frequently observed for the samples dialyzed with an electrolyte solution, the same electrolyte still gives different textures. This would be attributed to unavoidable fluctuations of ionic environments depending on the samples. In other words, real ionic conditions of nanosheets can be fluctuated from Debye length calculated by the concentration of the electrolyte solution. Thus, we measured electric conductivity of the colloidal samples after dialysis with electrolytes. The conductivity formation was examined at the concentration of 5 g L^{-1}. Relationships between the conductivity and RC values of the samples for each electrolyte species used for the dialysis indicate that the samples giving RC $\geq$ 1.5 are all in the conductivity range of 0.5 – 1.5 mS m^{-1}, as shown in Figure 5.3. The best quality stripes with RC $\geq$ 2 are obtained in the range of 0.6 – 1.0 mS m^{-1}. The requirement of the electric conductivity of colloids indicates that a certain amount of electrolyte must coexist in the nanosheet colloids for the "good stripe" formation, as indicated by moderate conductivities of the

81

samples. This fact suggests that electrical double layers at the nanosheet surfaces should not be too thick. This condition avoids long-range electrostatic repulsion between nanosheets to allow enough movement of the nanosheets. This state facilitates elongation and connection of the tactoids present in the sample prior to the electric alignment, and thus easily generates long stripes.

Figure 5.3. Ratio of Contrast (RC) values are plotted against electric conductivity for various electrolytes: (a) KCl, (b) C_3H_7Cl, (c) K_2CO_3, and (d) $C_3H_7NH_2$ solutions with 10^{-3} mol L^{-1}. For KCl system, the data for two more different concentration ranges are also plotted, lower than 5×10^{-4} mol L^{-1} and higher than 2×10^{-3} mol L^{-1}[17].

To explore common conditions for the formation of "good stripes" reflected by $RC \geq 1.5$, we measured pH of nanosheet colloids treated with electrolytes. Figure 5.4 summarizes relationships between the pH and RC values of the samples for each electrolyte species used for the dialysis. After the dialysis with KCl, $RC \geq 1.5$ is

obtained for the samples with pH between 7 and 9 (Figure 5.4a); more alkaline samples

with pH > 8 give RC ≥ 2.   This is almost the case for the samples dialyzed with

$C_3H_7NH_3Cl$ (Figure 5.4b).   Because this electrolyte gives weakly acidic solution by

hydrolysis, the colloid samples dialyzed by this species tend to produce somewhat acidic

conditions compared with the dialysis by KCl.   This would be the reason for the lower

probability of RC ≥ 1.5 with $C_3H_7NH_3Cl$ than that with KCl.   On the other hand, the

samples dialyzed by K_2CO_3 and $C_3H_7NH_2$, both of which tend to give more alkaline

conditions than KCl due to hydrolysis, indicate that pH higher than 9 is inappropriate in

most cases for the generation of stripes with RC ≥ 1.5 (Figure 5.4c, d).   These results
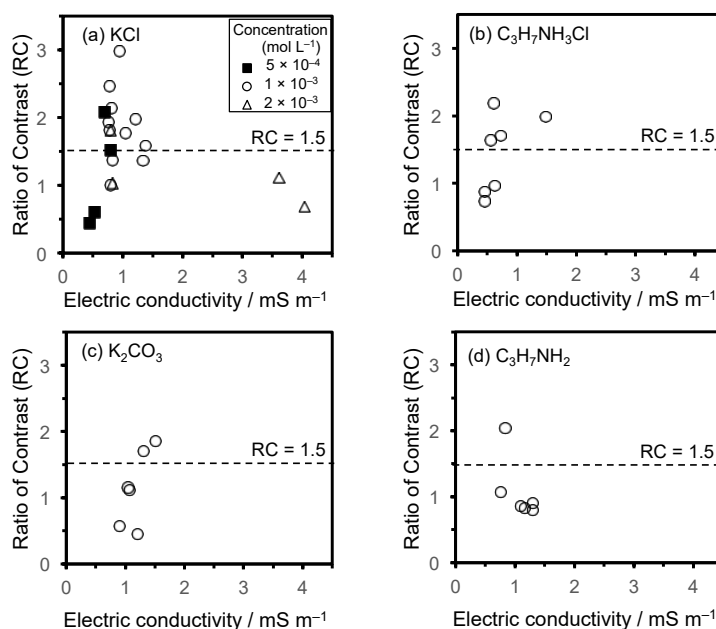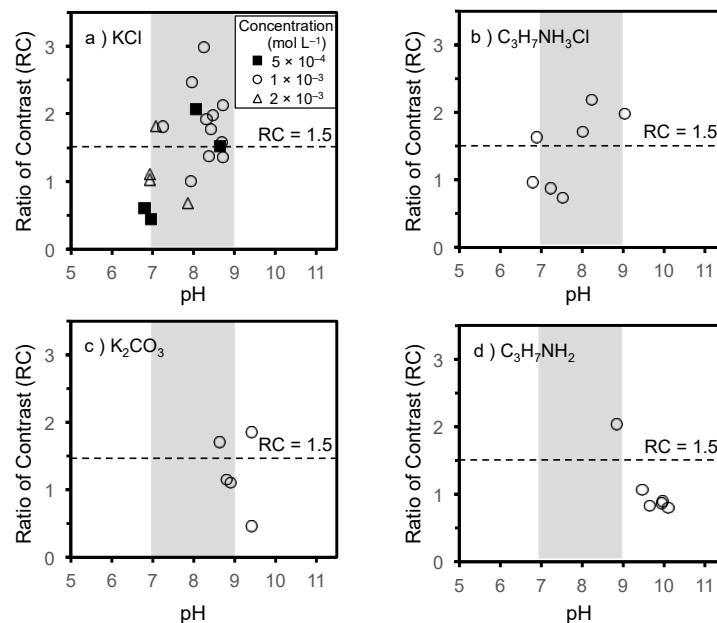

Figure 5.4. Ratio of Contrast (RC) values are plotted against pH for various electrolytes: (a) KCl, (b) C_3H_7Cl, (c) K_2CO_3, and (d) $C_3H_7NH_2$ solutions with 10^{-3} mol L^{-1}.   For KCl system, the data for two more different concentration ranges are also plotted, lower than 5×10^{-4} mol L^{-1} and higher than 2×10^{-3} mol L^{-1}[17].

indicate that the stripe texture with RC $\geq$ 1.5 is generated in weakly alkaline niobate nanosheet LCs in the pH rage of 7 to 9.   Moreover, best quality stripes with RC $\geq$ 2 are obtained at pH 8–9.

5.4. Summary

In this Chapter, the author has clarified the role of electrolytes in the linear alignments of nanosheet colloids to a macroscopic stripe generated in an AC electric field orthogonally applied to gravity.   Unidirectional alignment of nanosheets with high linearity is reflected by the formation of stripes, which are evaluated by RC values as described in Chapter 4.   Quality of the stripes are dependent of electrolytes introduced to the sample through dialysis, and "good" stripes are generated after dialyzing a nanosheet colloid with KCl: "poor" stripes, drops, or nets are obtained by dialysis with the other electrolytes examined or dialysis with pure water.   Dialysis with electrolyte solution modifies pH and conductivity of nanosheet colloids to influence particle–particle interactions.   This affects nanosheet fluidity in the colloid to alter the texture generated under the electric field.   With suitable electrolyte treatments to control colloidal environments into appropriate electric conductivity and pH ranges, the high linearity textures can be easily and reproducibly prepared.

References

1. . Nakato, Y. Nono, E. Mouri, M. Nakata. Panoscopic organization of anisotropic colloidal structures from photofunctional inorganic nanosheet liquid crystals. *Phys. Chem. Chem. Phys.*, 2014, **16**, 955-962.

2. Y. Nono, E. Mouri, M. Nakata, T. Nakato. Flow-induced assembly of colloidal liquid crystalline nanosheets toward unidirectional macroscopic structures. *J. Nanosci. Nanotechnol.*, 2016, **16**, 2967-2974.

3. N. Miyamoto, T. Nakato. Liquid crystalline nature of $K_4Nb_6O_{17}$ nanosheet sols and their macroscopic alignment. *Adv. Mater.,* 2002, **14**, 1267-1270.

4. T. Nakato, Y. Nono, E. Mouri. Textural diversity of hierarchical macroscopic structures of colloidal liquid crystalline nanosheets organized under electric fields. Colloids and Surfaces A: Physicochem. Eng. Aspects, 2017, **522**, 373-381.

5. B. B. Smith, D. Y. C. Chan, D. J. Mitchell. The electrostatic interaction in colloidal systems with low added electrolyte. *J. Colloid Interface Sci.*, 1985, **105**, 217-234.

6. A. M. EL Badawy, T. P. Luxton, R. G. Silva, K. G. Scheckel, M. T. Suidan, T. M. Tolaymat. Impact of environmental conditions (pH, ionic strength, and electrolyte type) on the surface charge and aggregation of silver nanoparticles suspensions. *Environ. Sci. Technol.*, 2010, **44**, 1260-1266.

7. E. S. Kooij, E. A. M. Brouwer, H. Wormeester, B. Poelsema. Ionic strength mediated self-organization of gold nanocrystals: An AFM study. *Langmuir*, 2002, **18**, 7677-7682.

8. J. Araki, S. Kuga. Effect of trace electrolyte on liquid crystal type of cellulose nanocrystals. *Langmuir*, 2001, **17**, 4493-4496.

9. L. Zhang, S. Fu, X. Peng, H. Zhan, R. Sun. Colloidal stability of negatively charged

cellulose nanocrystalline in aqueous systems. *Carbohydr. Polym.*, 2012, **90**, 644-649.

10. E. Paineau, I. Bihannic, C. Baravian, A. M. Philippe, P. Davidson, P. Levitz, S. S. Funari, C. Rochas, L. J. Michot. Aqueous suspensions of natural swelling clay minerals. 1. Structure and electrostatic interactions. *Langmuir*, 2011, **27**, 5562-5573.

11. H. Ohtaki. Ion No Suiwa (Hydration of Ions). *Kyoritsu Shuppan*, Tokyo, 1992.

12. A. T. Poortinga, R. Bos, W. Noide, H. J. Bsscher. Electric double layer interactions in bacterial adhesion to surface. *Surf. Sci. Rep.*, 2002, **47**, 1-32.

13. E. Tombacz, M. Szekeres. Colloidal behavior of aqueous montmorillonite suspensions: the specific role of pH in the presence of indifferent electrolytes. *Appl. Clay Sci.*, 2004, **27**, 75-94.

14. M. B. McBride, P. Baveye. Division S-2- "particle interactions in colloidal systems". *Soil Sci. Soc. Am. J.*, 2002, **66**, 1207-1217.

15. T.-Z. Shen, S.-H. Hong, J.-K. Song. Electro-optical switching of graphene oxide liquid crystals with an extremely large Kerr coefficient. *Nat. Mater.*, 2014, **13**, 394-399.

16. I. Dozov, E. Paineau, P. Davidson, K, Antonova, C. Baravian, I. Bihannic, L. J. Michot. Electric-field-induced perfect anti-nematic order in isotropic aqueous suspensions of a natural beidellite clay. *J. Phys. Chem. B*, 2011, **115**, 7751-7765.

17. J. Zhang, K. Morisaka, T. Kumamoto, E. Mouri, T. Nakato. Electrolyte-dependence of the macroscopic textures generated in the colloidal liquid crystals of niobate nanosheets. *Colloids Surf. A: Physicochem. Eng. Asp.*, 2018, **556**, 106-112.

Chapter 6. Conclusions

Chapter 6. Conclusions

In this thesis, the author reported the hierarchical assemblies of colloidal 1D and 2D particles in order to develop bottom-up fabrication of nanostructured materials. CNC nanorods and inorganic nanosheets have been employed as representatives of 1D and 2D particles, respectively.

In Chapter 1, the author described the background information about the hierarchical assembly of anisotropically shaped colloidal particles. In the beginning, the author introduced the significance of colloids particles. The use of anisotropic colloidal particles was emphasized because of their importance as building blocks of nanomaterials with structural asymmetry and functional gradient. The author described state-of-the-art in colloidal assemblies of CNCs and inorganic nanosheets. Based on these backgrounds, necessary future challenges for CNC nanorods and niobate nanosheets were presented as compartmentalization of nanostructures into chemically handleable sizes and development of quantitatively reproducible fabrication of nanostructures, respectively. Finally, the objectives of the present study were given.

In Chapters 2 and 3, the author reported compartmentalization of CNC nanorods as core-shell particles with polymers. The author adopted the self-organized precipitation (SORP) method as a simple method. With the SORP method, core-shell

particles were prepared in a system of two solutes and two miscible solvents.   The two solvents were good and poor solvents for both of the solutes.   When the good solvent was evaporated, the solubility of the solutes decreased, causing the formation of core-shell particles.   The particles architecture, i.e., the component location, was controlled by the difference in affinity of the two solutes to the poor solvent.   In the present study, the two solutes were CNC and PEG, and the two solvents were water and EG.   The affinity of PEG to EG, the poor solvent in our system, was controlled by changing its molecular weight: PEG2000 or PEG20000.   The core-shell particles with CNC core and PEG shell were prepared with PEF2000 because the affinity of this PEG to EG is higher than that of CNC.   In contrast the use of PEG20000, whose affinity to EG is lower than that of CNC, yielded the particles with CNC cores.   As a result, the author succeeded in small-scale compartmentalization of 1D-shaped colloidal particles via core-shell particle fabrications. Although there are other methods of preparing CNC-based core-shell particles, our method opens the way of tunable location of components in the assembled structures. The tunable micro-scale compartmentalization of anisotropic colloidal particles offers broad compartmentalized building blocks. This can facilitate the manufacture of novel micro-scale devices from the compartmentalization of anisotropic colloidal particles.

In Chapters 4 and Chapter 5, the author reported the hierarchical assembly of

niobate nanosheets into a unidirectional manner.　The nanosheets are assembled into a

stripe texture under an AC electric field applied orthogonally to the gravity.　First, the

author proposed a method quantitatively evaluate the unidirectionality of the assembly.

This was enabled by analyzing the POM images.　Contrast of the birefringent and dark

parts was as a measure of the nanosheet alignment, and the linearity of the stripes was

indicated by the ratio of the contrast along longitudinal and short directions.　By using

this method, the author evaluated the regularity and linearity of the nanosheet alignment

in niobate nanosheet colloids treated with various electrolytes.　Diversity of the textures

found in the colloids was successfully evaluated with the results of image analysis.

Electrolyte conditions for the unidirectional alignment with high regularity and linearity

were determined, and the found conditions were discussed in relation to the electrolyte

conductivity and pH of the colloids. As a result, the author succeeded in characterization

and reproducible preparation of macroscopically unidirectional structures from colloidal

nanosheets. This enables development of novel evaluation systems for particle assemblies

based on the characteristics of the aligned particles. Also, the reproducible assemblies of

macroscopic structures from colloidal particles can be achieved with careful control of

colloidal conditions. This enables preparation of macroscopically regular assemblies of anisotropic particles in board ranges.

On the basis of these individual findings, the author demonstrated in the present study that the tunable compartmentalization in small scale and reproducible assemblies of macroscopic structures with reliable characterization from anisotropic colloidal particles can be achieved. This enables hierarchically macroscopic assemblies of anisotropic colloidal particles into desired structures. It will enable the developments of multi-level advanced materials from anisotropic colloidal particle assemblies with easier strategies.

However, there are still many existed problems left for these anisotropic colloidal particle assemblies. They include i) expand compartmentalization into broader ranges of anisotropic colloidal particles; ii) develop a method to immobilize macroscopic colloidal structures; iii) discover protentional applications for assembled colloidal structures. This would ensure the efficiency of small-scale compartmentalization and it would be important for the enrichments of secondary building blocks from anisotropic colloidal particles. Also, studies about the retention or immobilization of macroscopic colloidal structures and their applications are hoped from both theoretical and practical aspects.

Achievement

1. Publications

(1) J. Zhang, H. Furushima, T. Nakato, E. Mouri. Preparation of cellulose nanocrystal based core-shell particles with tunable component location. *Chem. Lett.*, 2021, **50**, 240-243.

(2) J. Zhang, K. Morisaka, T. Kumamoto, E. Mouri, T. Nakato. Electrolyte-dependence of the macroscopic textures generated in the colloidal liquid crystals of niobate nanosheets. *Colloids Surf. A: Physicochem. Eng. Asp.*, 2018, **556**, 106-112.

2. International conferences

(1). Jie Zhang, Hinako Furushima, Emiko Mouri, Teruyuki Nakato. 8 [th] International Symposium on Applied Engineering and Sciences (SAES2020), Virtual Conference (2020).

Preparation of cellulose nanocrystal based shell-like structures with self-organized precipitation method.

(2) Jie Zhang, Emiko Mouri, Teruyuki Nakato. 12th Japan-Korea Joint Symposium on Biomicrosensing Technology (12th JKBT) –2nd Asian Symposium on Cutting-edge Biotechnology and Chemistry (ASCBC), Fukuoka, (2019).

Preparation of cellulose nanocrystals based core-shell particles via self-organized precipitation method.

3. National conferences

(1) Jie Zhang, Emiko Mouri, Teruyuki Nakato. Physical Chemistry Inter-College Seminar, Fukuoka, (2019).

Preparation of cellulose nanocrystals based core-shell particles.

(2) Jie Zhang, Keisuke Morisaka, Takuya Kumamoto, Emiko Mouri, Teruyuki Nakato. Japan MRS Annual Conference, Fukuoka, (2018).

Electrolyte-dependence of the macroscopic hierarchical organization of inorganic colloidal liquid crystals.

Acknowledgement

The accomplishment of present thesis is attributed to the helps and guidance from many persons as the author will thank below. Without their helps and guidance, the author cannot insist on finishing the present thesis. I really appreciate all their helps.

In the 5 years research period, the author really appreciates the guidance of his supervisor, Professor Nakato Teruyuki. With his patient and logical guidance in considering and writing aspects, the author is able to finish the present thesis and present thesis content. This kind of guidance will be the most valuable treasure in the author's later life.

Also, the author appreciates the helps and guidance from Associate Professor Emiko Mouri. Either in the research or daily life aspect, Associate Professor Emiko mouri has offered great helps and encouragements to the author for insisting on finishing the thesis. These helps will be important memories in the author's later life.

Also, the author really appreciates Professor Youichi Shimizu, Professor Masato Yamamura, Professor Koji Miyazaki, for their attendances for reviewing the author's thesis and their comments on revising the thesis with their valuable time.

Meanwhile, the author thanks Professor Shigeori Takenaka for permission of usage the Atomic Force Microscope and Mr. Noboru Wakayama for TEM characterization.

Meanwhile, the author really appreciates all the members in both Professor Nakato's group and Professor Shimizu's group. Their kindness gives me inner safety for insisting on the research.

Finally, I would like to thank all my family members for their understanding and supporting in my oversea studying.